JOURNAL OF GEOPHYSICAL RESEARCH, VOL. 105, NO. B5, PAGES 11,127–11,152, MAY 10, 2000

Plumes in a convecting mantle: Models and observations for individual hotspots

Bernhard Steinberger

Institut für Meteorologie und Geophysik, Johann Wolfgang Goethe-Universität, Frankfurt am Main, Germany

Abstract. The motion of hotspots and the deformation of their underlying plume conduits as calculated within models of global mantle flow are presented. A new list of 44 possible hotspots with associated tracks has been compiled. For all of them, calculations have been performed under consideration of individual age and anomalous mass flux for three different models of plume buoyancy and mantle flow. Plume source depth has usually been assumed to be the top of D", but an alternative source depth at the 670-km discontinuity has also been considered. Using models of relative plate motions and boundaries, hotspot tracks on plates have been calculated and compared with age data, ocean floor topography, and distribution of volcanics on continents. Absolute plate motions have been redetermined under consideration of hotspot motion, using a new least squares method. For the Hawaiian and Yellowstone hotspots, source locations and hotspot motion have been computed for a total of up to 23 different models. The results show plume conduits being tilted, with source regions at the D" moving in the lowermost mantle flow, generally toward large-scale upwellings under southern Africa and the south central Pacific. Hotspot surface motion often represents the horizontal component of midmantle flow, which is frequently opposite to plate motion, toward ridges and away from subduction zones. In particular, almost all models tested predict southward motion of the Hawaii and Kerguelen hotspots and westward motion of the Iceland hotspot. For models including hotspot motion the agreement between calculated and observed hotspot tracks is frequently about as good as, or better than, for the fixed hotspot model, but sometimes fixed hotspots give the best fit. In some cases where the track ends at a subduction zone, e.g., for the Bowie hotspot, results can give indications about the otherwise unknown age of the hotspot. In other cases, especially for the Tahiti hotspot, results suggest an origin shallower than D", and in yet other cases, particularly East Africa, the failure of the hotspot models used supports other evidence indicating the presence of comparatively broad upwellings rather than localized plumes.

1. Introduction

It has long been known [e.g., *Morgan,* 1971, 1972] that the relative motion of hotspots (small regions of intraplate volcanism unrelated to intraplate deformation, or especially vigorous volcanism along plate boundaries) is much slower than the motion of plates. Hotspots have therefore been used as a reference frame for plate motions. However, the plumes that are thought to cause hotspots arise from a convecting mantle whose flow is evident through the motion of the tectonic plates. Thus hotspots should not be expected to be absolutely stationary. "Hotspot fixity" on a global scale has not been universally agreed on [e.g., *Molnar and Stock,* 1987], and more recent data (e.g., by *McNutt et al.* [1997] for the Southern Austral Islands thought to be associated with the Macdonald plume and compiled by *Schmincke* [1982] for the volcanics in central Europe thought to be associated with the Eifel plume) show that the age progression along presumed hotspot tracks (chains of seamounts or aseismic ridges in the oceans and areas of intraplate volcanism on continents that form as the plate moves over the hotspot) is often not as regular as presumed in the early days of plume theory (e.g., by *Morgan* [1971, 1972] for the Austral Island chain and by *Duncan et al.* [1972] for the Eifel plume). A mantle plume in the classical sense, a narrow upwelling from deep inside the Earth, as originally proposed by *Wilson* [1963], may therefore often not even be a good explanation for intraplate volcanism. Other possible sources include incipient continental rifting, such as in East Africa, and other intraplate stresses [e.g., *Sleep,*

Paper number 1999JB900398.
0148-0227/00/1999JB900398$09.00

1990] or local melting anomalies beneath the ocean floor [e.g., *Hofmann,* 1997].

This paper attempts to contribute to an understanding of observed hotspot tracks and other forms of intraplate volcanism in the context of dynamic Earth models. Model calculations of plumes have been performed and the results compared with surface observations. This approach should help to bridge the gap between numerical models of the Earth's mantle and observations of geological and morphological features on Earth's surface.

In previous work [*Steinberger,* 1996; *Steinberger and O'Connell,* 1998] a model of the Earth's mantle which allows for motion of hotspots but nevertheless yields tracks which are compatible with observations has been presented. However, the focus was on the general characteristics of the model, and specific tracks were presented only for a few selected hotspots. This paper looks at individual, actual hotspots: In order to cover the topic both comprehensively and in depth a threefold approach is used.

First, a list of hotspots has been compiled. Source location in D", conduit shapes, and surface motion have been calculated for all 44 of these hotspots using three different mantle models. The similarity of results among the three models in most cases already indicates that the results do not depend on a specific model. Second, in cases where a narrow track and/or a clear age progression is observed, such as to merit comparison, calculated hotspot tracks on plates are shown. Thus it is shown that the calculations including hotspot motion can explain hotspot tracks just as well as those using the fixed hotspot hypothesis. Third, the robustness of the results and their dependence on various parameters are discussed by considering a greater number of models for the Hawaiian and Yellowstone hotspots.

2. Modeling Hotspot Motion

Previously, hotspot tracks have been calculated for given plate motions, assuming hotspots are fixed; plate motions have often been determined by obtaining a good fit between observed and calculated hotspot tracks under this assumption. In this work, no assumption of hotspot fixity is made; instead, the motion of hotspots has been calculated from the advection of plumes in a realistic mantle flow field. The modeling procedure was previously discussed in detail by *Steinberger and O'Connell,* [1998]. Thus only a brief description is given here, focusing on the specific features of the models in this paper.

2.1. Calculation of Mantle Flow

Explicit low-resolution tomographic models of mantle density have recently been presented [*Kuo et al.,* 1998; *Ishii and Tromp,* 1999]. More traditionally, density heterogeneities have been inferred from tomographic s wave models, and *Ishii and Tromp* [1999] also show that shear modulus and density are correlated at a high confidence level throughout most of the mantle. For the three mantle models mainly discussed in this paper, this more traditional approach is followed: Density anomalies are inferred from S12WM13 [*Su et al.,* 1994] for mantle models 1 and 2, and S. Grand's model (as of November 1998, similar to that of *Grand et al.* [1997]; the latest version is available at amazon.geo.utexas.edu) for mantle model 3. For S12WM13 a conversion factor $(\delta\rho/\rho) \,/\, (\delta v_s/v_s) = 0.2$ from seismic velocity to density heterogeneities has been used. For Grand's model a value of 0.4 has been used to compensate for the lower amplitudes of this model. Both numbers are close to those inferred from geoid modeling [e.g., *Forte et al.,* 1993] and from laboratory experiments in combination with theoretical arguments [*Karato,* 1993]. For the three mantle models 1–3, only density heterogeneities below 220 km depth have been used in order to at least partly exclude effects of compositional continental roots. In section 6, results for some other density models are also shown.

The density heterogeneities cause the driving forces of mantle flow. Because it is slow, mantle flow is governed by the "Navier-Stokes" equation of motion (relating velocities and stresses) without the inertial term. A Newtonian viscous rheology has been assumed. Furthermore, conservation of mass and the Poisson equation relating gravity and density have to be satisfied. Boundary conditions are the given surface plate velocities (which will be discussed in section 5.1.1) and a stress-free core-mantle boundary. The equations were solved using the method of *Hager and O'Connell* [1979, 1981]. This method uses spherical harmonic expansions of surface plate velocities and internal density heterogeneities at certain depth levels in order to calculate the flow separately for each spherical harmonic degree and order. With this technique the governing equations of flow are reduced to a set of ordinary differential equations which can be integrated in radial direction. The flow field was expanded up to degree and order 15 when using a lower-resolution tomographic model such as S12WM13 and to degree and order 31 when using a higher-resolution model such as Grand's. The method has been described in more detail by *Steinberger and O'Connell* [1998, Appendix A1].

The flow code has been modified to include compressibility: The mantle was divided into a number of layers of constant density based on the Preliminary Reference Earth Model (PREM) [*Dziewonski and Anderson,* 1981]. All internal density jumps were assumed to be related to compressibility, with boundary conditions given by *Panasyuk et al.* [1996, equation (40)]. Effects of two phase boundaries at depths of 400 km and 670 km were also included: Density anomalies were converted to sheet mass anomalies using conversion factors 132 km at depth 400 km and -58 km at depth 670 km, based on work by *Akaogi et al.* [1989] and *Akaogi and Ito* [1999]. The effect of phase boundaries on the flow field was found to be small.

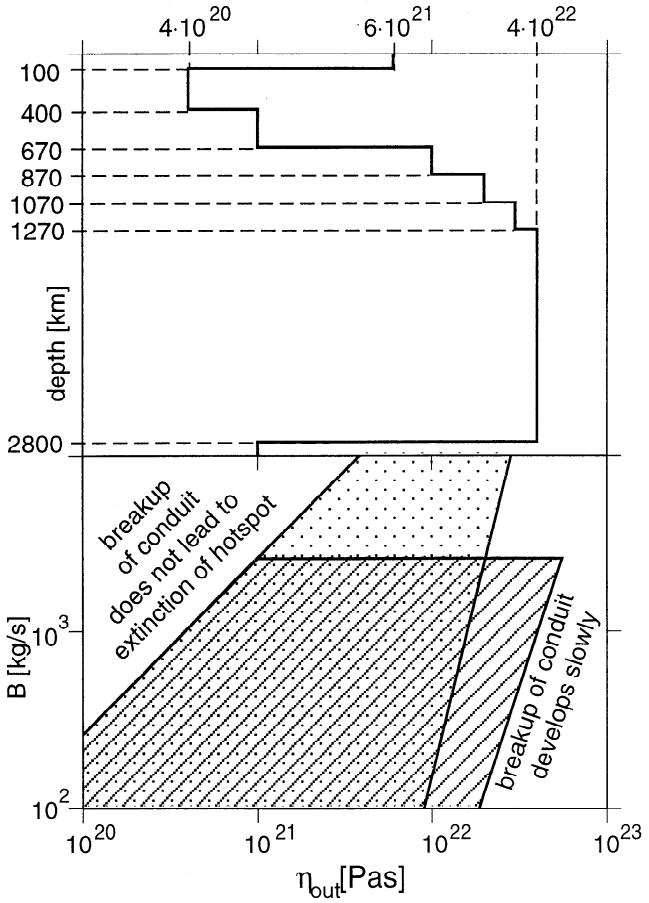

Figure 1. (top) Ambient mantle viscosity structure used. (bottom) An estimate of the viscosity range for which a tilt of the conduit of $> 60°$ would lead to extinction of a plume within $\lesssim 100$ Myr for mantle models 1 (stippled) and 2 and 3 (striped). The regions are defined by the relations $2r_c/u < 100$ Myr (i.e., breakup will develop sufficiently fast) and $u < 2l\kappa/r_c^2$ (i.e., breakup of a conduit of length l in a medium of diffusivity κ will lead to extinction, as previously estimated by *Steinberger and O'Connell,* [1998]), using equations (1), (3), and (4) with $\Delta\rho = 30$ kg/m^3, $g = 10$ m/s^2, $l = 2700$ km, $\kappa = 1.2 \times 10^{-6}$ m^2/s.

The flow field was also used to advect the density heterogeneities, which drive the flow, back in time to 68 Ma; we have previously described the advection in more detail and have estimated that the approximations made in this procedure (neglecting diffusion, viscous dissipation, adiabatic heating and cooling effects) can be justified for this time period, for the purpose of calculating the motion of hotspot plumes [*Steinberger and O'Connell,* 1998, Appendix A2]. Before 68 Ma, density anomalies were left constant. The time history of maximum density heterogeneities in each radial layer was monitored to ascertain that no runaway instabilities develop.

2.2. Radial Mantle Viscosity Structure

The viscosity structure mainly used is shown in Figure 1 and is based on inferences from postglacial rebound and the geoid: Between 100 and 870 km depth it follows the model by *Lambeck and Johnston* [1998] and is also in agreement with results by *Mitrovica* [1996], based on postglacial rebound data.

Compared to our preferred structure [*Steinberger and O'Connell,* 1998], the minimum viscosity in the upper mantle has been increased by about a factor of 3, whereas the maximum viscosity in the lower mantle has been decreased by about a factor of 3, reducing the viscosity contrast between upper and lowermost mantle from about a factor of 800 to 100, thus making it more compatible with models of the geoid, as elaborated below. It was possible to assume a higher viscosity in the upper mantle only by also using higher buoyant rising speeds of the conduits. They would otherwise become strongly distorted in the upper mantle. Despite the reduced viscosity in the lowermost mantle, flow speeds have remained very similar, in part due to considering compressibility, which decreased flow speeds in the lowermost mantle by ~20 %.

The relation between geoid and mantle density heterogeneities in a dynamic Earth was derived by *Ricard et al.* [1984] and *Richards and Hager* [1984]. More recently, a model with constant viscosity in the upper mantle, a lithosphere with 10 times upper mantle viscosity, and a lower mantle with 50 times upper mantle viscosity has been used to optimize the fit to the geoid and to explain dynamic topography [*Ricard et al.,* 1993; *Lithgow-Bertelloni and Silver,* 1998]. Here, viscosities in the lithosphere and below 870 km were chosen such that geoid kernels (calculated with a code written by S. Panasyuk and described by *Panasyuk et al.* [1996]) are very similar to such a model result. Other recent models of mantle viscosity based on the joint inversion of convection and postglacial rebound observables also feature a "significant increase of viscosity (~ 2 orders of magnitude), with depth" [*Mitrovica and Forte,* 1997, p. 2751]. Similar to the approach presented here, a high-viscosity lower mantle has been previously inferred from models of hotspot motion [*Richards,* 1991], and it has been shown that a low viscosity in the upper mantle is required to explain the sharp bend in the Hawaiian-Emperor chain [*Griffiths and Richards,* 1989].

2.3. Calculation of Plume Conduit and Hotspot Motion

The motion of a conduit was calculated assuming that the velocity of each part of the conduit is equal to the sum of the mantle flow velocity at the same location and the vertical buoyant rising velocity u. The location of the point where the conduit intersects the bottom of the lithosphere (assumed to be at a depth of 100 km) as a function of time is shown as "hotspot surface motion," assuming that magma rises more or less vertically through the lithosphere. An iterative minimization scheme was used to search for initial plume locations yielding agreement of actual and calculated present plume locations. Two different models of the

plume source were used: In most cases, source model A, corresponding to a plume conduit being established by a large plume head rising from D", the "standard plume model," was used. In some cases, a plume without head rising from 670 km depth (source model B) was assumed.

2.3.1. Models for the buoyant rising speed of conduit elements. The rising speed u is related to the radius r_c of the conduit through a modified Stokes' formula:

$$u = \frac{k_c \Delta\rho g r_c^2}{\eta_{\text{out}}}. \quad (1)$$

This is the rising speed of the conduit though the surrounding mantle and must not be confused with the speed at which material flows through the conduit. A value $k_c = 0.54$ was used, following experiments by *Richards and Griffiths* [1988] for a chemical plume (although the value for a thermal plume may be higher). $\Delta\rho$ is the density contrast between plume and surroundings, g is gravity, and η_{out} is the viscosity of the surrounding mantle (see Figure 1). Poiseuille's formula for flow in a pipe can be used to relate r_c and anomalous mass flux B [e.g., *Turcotte and Schubert*, 1982]:

$$r_c = \left(\frac{8B\eta_{\text{in}}}{\pi\Delta\rho dp/dz}\right)^{\frac{1}{4}}, \quad (2)$$

where η_{in} is the viscosity inside the conduit and dp/dz is the nonhydrostatic pressure gradient driving flow through the conduit.

By combining (1) and (2) it follows that

$$u = \frac{k_c \Delta\rho g}{\eta_{\text{out}}} \sqrt{\frac{8B\eta_{\text{in}}}{\pi\Delta\rho dp/dz}}.$$

On the basis of this equation, it was assumed for mantle model 1 in the entire mantle and for mantle models 2 and 3 if $\eta_{\text{out}} \leq 10^{21}$ Pa s, that

$$u = u_0\sqrt{B/B_0}\ \eta_0/\eta_{\text{out}}, \quad \eta_{\text{in}} = \text{const}, \quad (3)$$

and for mantle models 2 and 3 and $\eta_{\text{out}} \geq 10^{21}$ Pa s it was assumed that

$$u = u_0\sqrt{B/B_0}\ \sqrt{\eta_0/\eta_{\text{out}}}, \quad \eta_{\text{in}} \propto \eta_{\text{out}}, \quad (4)$$

with $B_0 = 10^3$ kg/s, $\eta_0 = 10^{21}$ Pa s, and $u_0 = 2$ cm/yr.

The assumption $\eta_{\text{in}} \propto \eta_{\text{out}}$ may be more appropriate if the depth dependence of temperature is adiabatic both inside and outside the conduit; it was not used in the uppermost mantle (asthenosphere), where flow speeds are fastest, in order to achieve a higher rising speed and prevent conduits from becoming strongly tilted and because the asthenosphere may, at least partly, be fed by plumes [*Phipps Morgan et al.*, 1995].

2.3.2. Plume source model A. The large head of a plume rising from D" would rise much faster than the narrow conduit: The initial condition is therefore a vertical conduit at a time equal to the assumed age of the hotspot (see Table 1). This source model has been used and justified by *Steinberger and O'Connell* [1998]. It is based on theoretical, numerical, and experimental results and is supported by observations on the Earth surface: Theoretical considerations show that a thermal boundary layer inside the Earth (core-mantle boundary or 670-km discontinuity) gives rise to instabilities [*Loper and Stacey*, 1983]. Both numerical and experimental results show that if the viscosity inside the instability is significantly lower than outside, it takes the shape of a large "plume head" followed by a narrow conduit [*Whitehead and Luther*, 1975; *Manga et al.*, 1993]. A relation between flood basalts and the initiation of hotspots has been suggested [*Morgan*, 1981], and it has subsequently been postulated that large flood basalts represent plume heads [*Richards et al.*, 1989; *Campbell and Griffiths*, 1990]. Many volcanic chains (island and seamount chains in the oceans, linear arrays of volcanics on continents) with active volcanism on one end and age progressively getting older toward the other end of the chain are seen as expressions of the conduit over which the plate moves [*Morgan*, 1971, 1972].

An experimentally determined equation for the risetime t of the plume head through a layer of thickness d has been reported by *Richards et al.* [1989] where

$$t = (d/0.16)^{5/7}(\eta_{\text{out}}/g\Delta\rho)^{4/7}(B/\Delta\rho)^{-3/7}.$$

Results by *Griffiths and Campbell* [1990] are in accordance with this. In deriving this formula the assumption was made that the plume head is growing at the same rate at which material is flowing through the conduit. With $\Delta\rho = 30$ kg/m^3, $g = 10$ m/s^2, $\eta_{\text{out}} = 4 \times 10^{22}$ Pa s and d=2130 km, this gives times to penetrate the lower mantle of between ~100 Myr for the biggest plumes and ~500 Myr for the smallest plumes. This would imply that especially for smaller plumes, conduits are expected to be severely distorted already at the time the plume head reaches the base of the lithosphere [*Griffiths and Campbell*, 1990]. However, these estimates should be regarded as upper boundaries. *Richards et al.* [1989] point out that only a fraction of the head may actually be fed through the conduit, which would imply much shorter risetimes. In this case, the equation for the Stokes speed of an inviscid sphere [e.g., *Batchelor*, 1967],

$$u_{\text{head}} = \frac{\Delta\rho g r_{\text{head}}^2}{3\eta_{\text{out}}}$$

would be more appropriate. Taking $r_{\text{head}} = 500$ km as a typical estimate [e.g., *Griffiths and Campbell*, 1990], rise times of < 100 Myr would result. On the basis of the root mean square differences in horizontal flow speed between the lowermost mantle above D" and at shallower depths, an initial horizontal deflection of the conduit of ~800 km is estimated in this case. Plumes may rise even faster if temperatures are higher, producing lower than average viscosities in the vicinity of the

Table 1. List of "Hotspots" Used

	Hotspot Name	Volcanic Feature	Age, Ma	$B, 10^3$kg/s	Lat	Long	Features
1	Azores	Pico	100.[b]	1.2	38.5	-28.4	1,2
2	Balleny	Buckle Island	36.[b]	---	-66.8	163.3	1,2
3	Bowie		30.[c]	0.6	53.	-135.	1,2,3
4	Cameroon	Cameroon Mountain	31.[b]	---	4.2	9.2	1,2
5	Canary		65.[b]	1.0	28.	-18.	1,2
6	Cape Verde		20.[b]	1.1	15.	-24.	1,2
7	Caroline		80.[c]	1.6	5.	164.	2,3
8	Cobb	Axial Seamount	43.[c]	0.3	46.0	-130.0	1,2,3
9	Comores	Karthala	63.[b]	---	-11.8	43.3	1,2
10	Darfur		140.[b]	0.4	13.	24.	1,2,3
11	East Africa		40.[a]	1.1	6.	34.	1,4
12	East Australia		50.[c]	0.9	-38.	143.	1,3
13	Easter	Easter Island	100.[c]	2.1	-27.1	-109.3	1,2,3
14	Eifel		40.[b]	---	50.	7.	1,3
15	Fernando		201.[a]	0.7	-4.	-32.	2,3
16	Galapagos	Isla Fernandina	85.[a]	1.4	-0.4	-91.5	1,2,4
17	Guadelupe		25.[c]	0.3	27.	-113.	2,3
18	Hawaii	Kilauea	100.[c]	6.5	19.4	-155.3	1,2,3
19	Hoggar		20.[b]	0.6	23.	6.	1,2
20	Iceland		60.[a]	1.2	65.	-19.	1,2,4
21	Jan Mayen	Beerenberg	210.[a]	0.6	71.1	-8.2	1,2,4
22	Juan Fernandez		30.[c]	1.7	-34.	-82.	2.3
23	Kerguelen		117.[a]	0.9	-49.	69.	2,3,4
24	Lord Howe		50.[c]	0.9	-33.	159.	2,3
25	Louisville		120.[a]	2.0	-51.	-138.	2,3,4
26	Macdonald	Macdonald Seamount	120.[c]	3.6	-29.0	-140.2	1,2,3
27	Marion	Marion Island	195.[a]	---	-46.9	37.8	1,2,3,4
28	Marquesas		9.[b]	3.9	-11.	-138.	2,3
29	Meteor		120.[b]	0.5	-52.	1.	1,2,3
30	New England		120.[b]	0.4	28.	-32.	2,3
31	Pitcairn		8.[b]	2.5	-25.	-129.	1,2,3
32	Raton		20.[b]	---	37.	-104.	1,3
33	Reunion	Piton de la Fournaise	67.[a]	1.4	-21.2	55.7	1,2,3,4
34	St Helena		100.[b]	0.4	-17.	-10.	2,3
35	Samoa		14.[b]	1.6	-15.	-168.	1,2
36	San Felix		30.[c]	1.9	-26.	-80.	2,3
37	Socorro	Socorro Island	25.[c]	0.5	18.7	-111.0	1,2
38	Tahiti	Mehetia	5.[b]	4.5	-17.9	-148.1	1,2,3
39	Tasmanid		50.[c]	0.9	-39.	156.	2,3
40	Tibesti		80.[c]	0.3	21.	17.	2,3
41	Trindade	Martin Vas	65.[b]	0.7	-20.5	-28.8	1,2,3
42	Tristan		125.[a]	1.0	-38.	-11.	1,2,3,4
43	Vema		40.[b]	0.4	-33.	4.	2,3
44	Yellowstone		15.[a]	1.5	44.6	-110.5	1,3,4

Names, with volcanic features used to define location, age estimates, anomalous mass fluxes B, locations (lat, long), and features (according to enumeration in text) of hotspots are given. Estimates of anomalous mass flux are based on work by *Davies* [1988], *Sleep* [1990], *Schilling* [1991], *Davies* [1992], and *Ribe and Christensen* [1999]. Where no estimate has been given in any of these papers, a value of 0.5×10^3 kg/s was used in the calculations. Location is usually given to 0.1° accuracy if it is chosen to coincide with a particular volcanic feature; otherwise to 1°. Present and Holocene volcanic activity has been compiled from *MacDonald* [1972], *McClelland et al.* [1989], and *Epp* [1984].

[a]Ages of associated flood basalts are used.

[b]The measured or estimated (according to length of track) oldest age on the track is taken.

[c]An educated guess is made because part of the track may have been subducted.

plume head. If the rheology is nonlinear, large stresses surrounding the plume head may also decrease the effective viscosity [*Larsen and Yuen*, 1997; *van Keken*, 1997]. Because plumes occur frequently in regions of a hot ambient mantle, they may be further helped in their ascent by large-scale rising flow. Given all this, and the fact that many hotspots are assumed to be rather old (hence the mantle flow through which the plume head has risen is rather poorly known), an initially vertical conduit is a justifiable assumption.

2.3.3. Plume source model B. Some hotspots, which are not associated with flood basalts, are more closely spaced than one would expect for upwellings from the CMB and are associated with rather short tracks. It may therefore be more appropriate to assume a plume starting at the 670-km discontinuity. In particular, the Pacific plate is dotted with thousands of seamounts, and it is hard to imagine that all of these originate from plumes rising from the core-mantle boundary; a more shallow origin for a large fraction of them seems much more plausible. A large plume head may not be required in order to penetrate a low-viscosity upper mantle. Source model B therefore corresponds to a plume without head: all conduit elements start at the depth of the 670-km discontinuity such that the conduit is already tilted when the plume first reaches the lithosphere. Again, the plume source moves with the horizontal flow component at the source depth. For source model B the calculation is required to start at a time somewhat greater than the assumed age of the hotspot, such that conduit elements have already reached the surface at the time equal to the assumed age of the hotspot. Calculated hotspot motion at a given time for a given present location is independent of the assumed age, in contrast to source model A.

3. A List of Hotspots

The active volcanism on Reunion, in combination with the progressively older volcanism of the Mascarene and Maldives tracks and a flood basalt in the Deccan traps, gives a perfect example of a hotspot track. Unfortunately, the situation is less clear in many other cases: Many areas described as hotspots are not associated with flood basalts, and the linear volcanic chain frequently does not have a clear age progression. The list of hotspots presented here is therefore based on circumstantial evidence: Since the calculated tracks are to be compared with observations, only locations which are associated with a volcanic chain, or where at least two age data differing by several million years are available, have been included. In order to exclude other kinds of volcanism, I exclude subduction zones and require at least two of the following features: (1) present-day or recent volcanism, (2) distinct topographic elevation, (3) associated volcanic chain, or (4) associated flood basalt. The list presented in Table 1 is also based on the works by *Morgan* [1981], *Richards et al.* [1988], and *Duncan and Richards* [1991]. Owing to the selection criteria, the list does not include any of the locations in Asia shown by *Burke and Wilson* [1976]. This does not mean there are no hotspots in Asia; they may just be difficult to recognize. Conversely, many of the hotspots included in the list may not have a deep origin. Locations, anomalous mass flux, and association with flood basalts of hotspots are also shown in Figure 2.

4. Results for Plume Conduits and Hotspot Motion

4.1. Plume Source Locations and Conduit Shape

Figures 3 and 4 show plume conduits for source model A. Also shown is the calculated present horizontal flow component at the top of D". Although results differ somewhat for the various mantle models, there is a general tendency for plumes to be tilted, with source re-

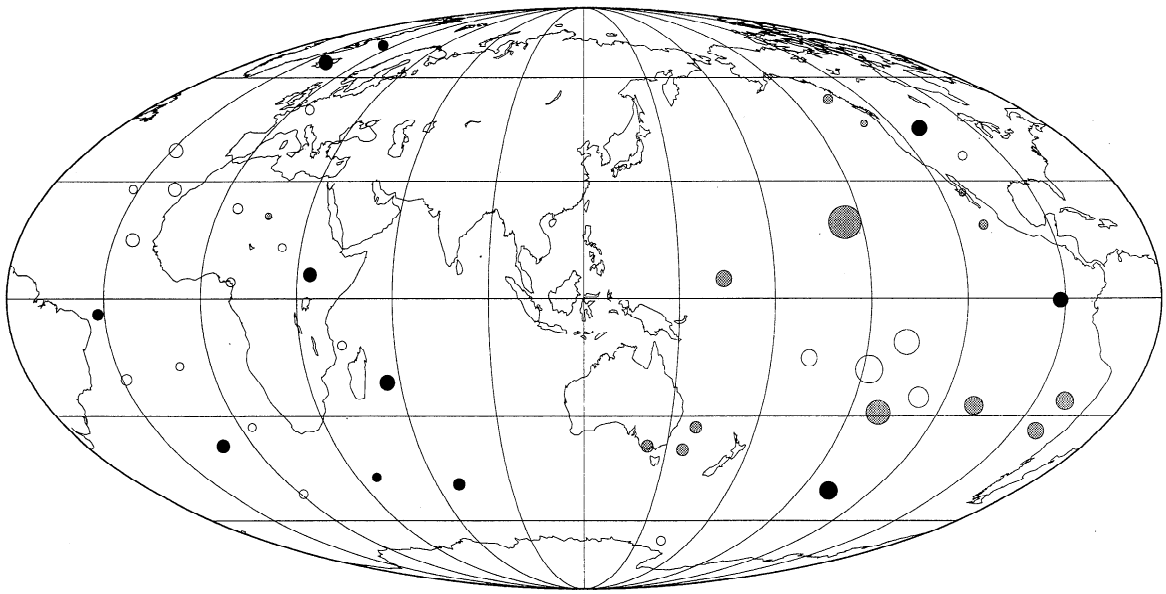

Figure 2. Global distribution of hotspots according to Table 1. Shading indicates whether hotspots are associated with flood basalts (black, yes; white, no; grey, not known, since the end of the track may have been subducted). Area of circle corresponds to the magnitude of the anomalous mass flux.

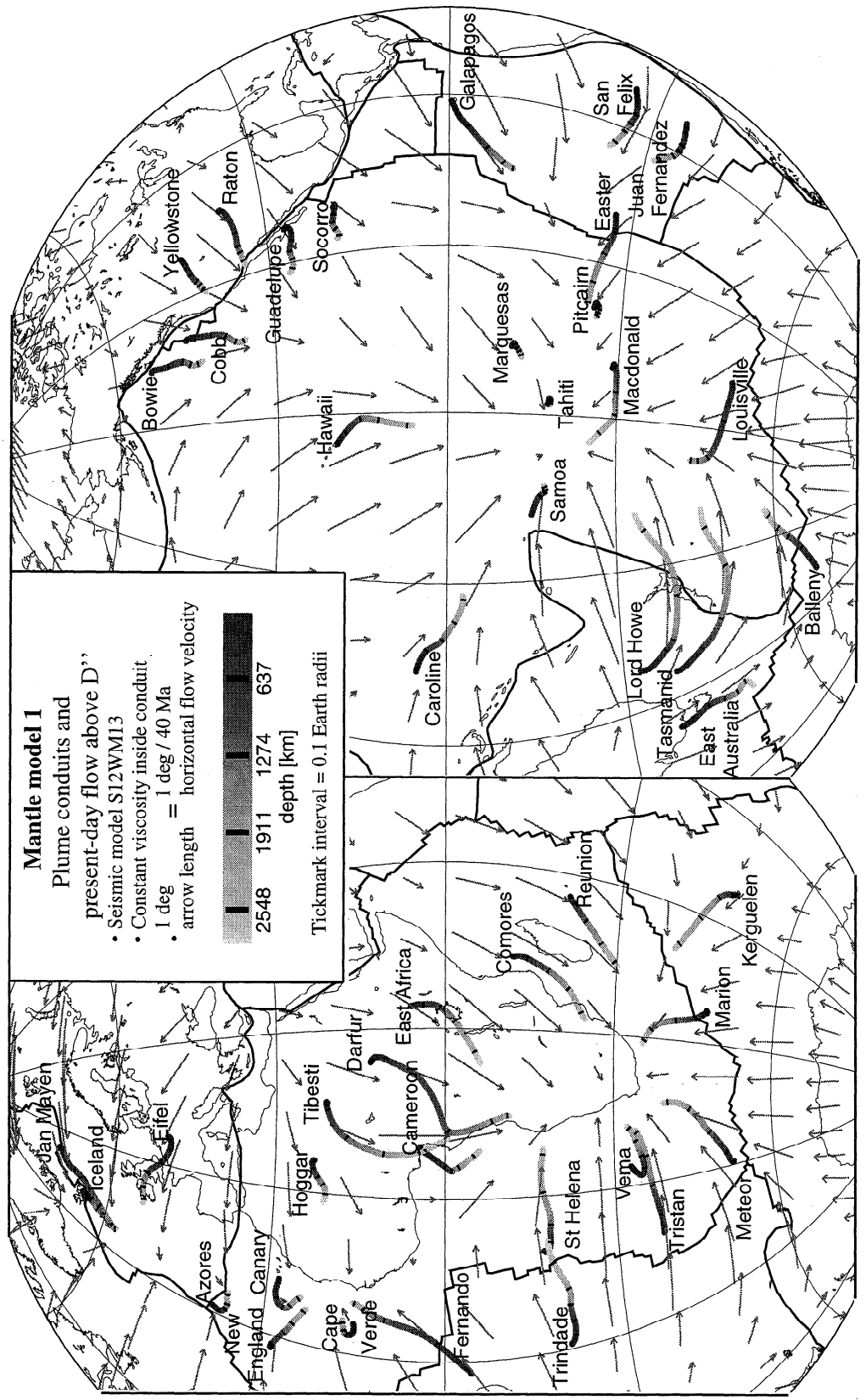

Figure 3. Plume conduits and present-day flow above D'' for mantle model 1.

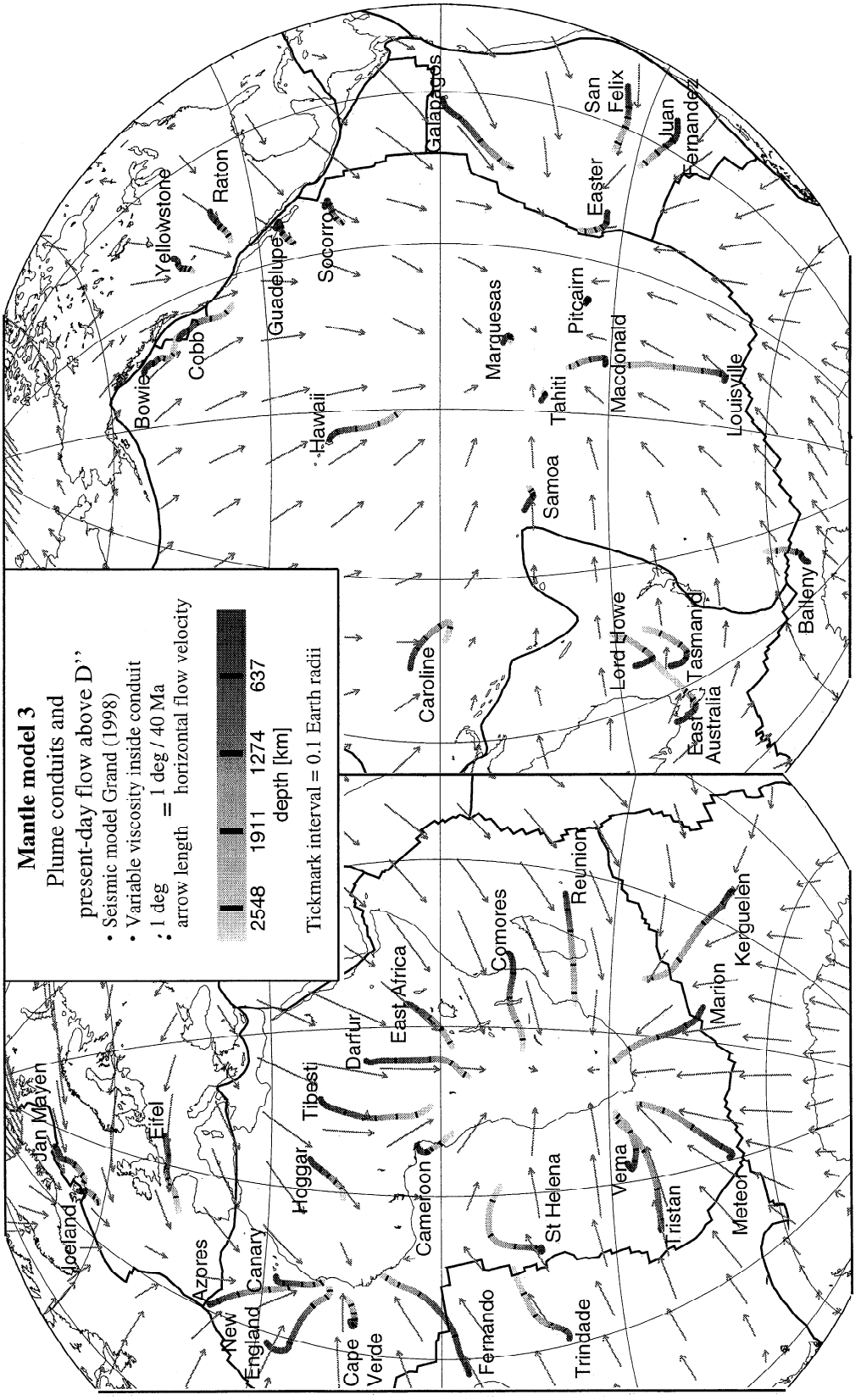

Figure 4. Plume conduits and present-day flow above D'' for mantle model 3.

gions clustering around the two large upwellings even more strongly than surface locations. Older plumes tend to be tilted stronger than younger ones. This occurs because the bases of the plumes get advected with the flow toward the large upwellings in the models, whereas hotspot surface motion tends to be influenced more by the flow at shallower depth, which may be in a different direction.

In the mainly used two mantle flow models, viscosity increases by a factor of 100 throughout the mantle, and root mean square amplitudes of flow speed drop by a factor of 3.6 and 3.9 between the surface and above D". According to *Gurnis* [1986], and also emphasized by *Richards* [1991] and *Ricard et al.* [1993], flow speeds should decrease inversely proportional to the logarithm of viscosity increase, therefore, in this case, by about a factor of ln(100)=4.6. However, the amplitudes of the wave speed anomalies in the tomographic models tend to increase toward the core-mantle boundary (CMB), especially at low spherical harmonic degrees, which are the most effective in driving the flow, therefore leading to a somewhat smaller drop in root mean square flow speed amplitudes, which are even slightly larger above D" than at a depth of 670 km.

The predicted plume source locations for three mantle models are also listed in Table 2. For mantle models 1 and 2, which use the same mantle flow field, the results are very similar, reflecting that conduit motion in the lower mantle is dominated by advection rather than buoyant rising. For the same reason, conduit shapes are also very similar for the two mantle models; they are therefore only shown for model 1 in Figure 3. Of particular interest are the predictions for Hawaii and Iceland, as detailed seismological investigations of the D" layer beneath these hotspots have recently been performed [*Russell et al.,* 1998; *Helmberger et al.,* 1998]. Below Iceland, *Bijwaard and Spakman* [1999] also show tomographic evidence for a narrow whole mantle plume.

4.2. Tilts of Plume Conduits

Table 2 also lists the maximum tilts achieved over the lifetime of a plume. According to *Whitehead* [1982], conduits should become unstable when tilted more than 60° from the vertical. However, a plume may survive despite a tilt > 60° if the tilt either occurs in a surrounding mantle of sufficiently high viscosity, such that the instability will develop slowly, or sufficiently low viscosity, such that conduit fragments will rise sufficiently fast to enable enough material to flow through the intact conduit underneath and thus prevent extinction (see Figure 1). The results indicate that tilts are often substantial. In most cases, however, calculated tilts do not, or only slightly, exceed 60°. Tilts that exceed 60° significantly can occur if a hotspot is assumed to be rather old (such as Darfur, where the age estimate is given by *Garfunkel* [1992]) or is close to a subduction zone and hence severely distorted by the associated downward flow (such as Galapagos, which has been associated by *Richards et al.* [1989] with the 85 Ma Caribbean Flood Basalts). Conduits also become strongly sheared and tilted if flow varies strongly with depth in the midmantle, such as in the vicinity of the hotspots on the Australian plate for both mantle models 1 and 2. For other hotspots (St. Helena, New England), where the most recent volcanic activity occurred 10 Myr ago or longer [*Morgan,* 1981; *Duncan,* 1984], the large tilt angles in excess of 60° may be responsible for the recent extinction.

4.3. Motion of Hotspots

Figures 5 and 6 show hotspot surface motion, again for source model A, along with the horizontal flow component at the depth of 670 km. Owing to the different radii at which flow fields are shown in Figures 3–6, arrows in Figures 5 and 6 correspond to faster flow speeds (in cm/yr) than arrows of equal length in Figures 3 and 4. Averages of recent hotspot motions are also listed in Table 2. Again, results for mantle models 1 and 2 are very similar; therefore hotspot motions for mantle model 2 are not shown in a figure.

In many areas of the upper part of the lower mantle the flow models show a plate return component flowing in the opposite direction to plate motions, toward ridges and away from subduction zones [see also *Steinberger and O'Connell,* 1998]. *Steinberger and O'Connell* [1998] also presented a very simple model without time dependence, vertical flow, or lateral variations and a plume source in D" (corresponding to source model A). In that model, hotspot surface motion always represents horizontal flow at a certain depth. This depth increases with time at a rate equal to the buoyant rising speed at that depth. For the mainly used viscosity model (Figure 1), it should therefore be expected that during a rather short initial period (a few million years) after the plume head has reached the lithosphere, hotspot motion represents flow at shallow levels (up to ~400 km). Following this, hotspot motion should mirror the flow in the midmantle (upper part of the lower and lower part of the upper mantle) for rather extended time periods. Flow in the lowermost mantle should have no influence on hotspot surface motion at all. Figures 5 and 6 show that the calculated recent hotspot surface motion is often similar to flow at midmantle depths. If younger age and/or small buoyancy is assumed (e.g., for the hotspots on the Australian plate or Yellowstone), the calculated motions tends to represent flow at shallower levels than for old age/high buoyancy plumes (e.g., Hawaii). Surface motion is in part also due to the tilt of the conduit because the locations from where conduit elements rise to the surface change with time.

An analogous simple model without vertical flow, time dependence, or lateral variation and a plume source at depth 670 km (corresponding to source model B)

Table 2. Predicted Plume Locations at the Top of D", Calculated Hotspot Motion, and Maximum Tilt Angle for Three Models

	Mantle Model 1				Mantle Model 2				Mantle Model 3			
	Lat	Long	$\bar{v}$	Tilt, deg	Lat	Long	$\bar{v}$	Tilt, deg	Lat	Long	$\bar{v}$	Tilt, deg
1	36	-24	5S41W	22(51)	37	-24	5S34W	18(52)	25	-19	2S36W	43(51)
2	-58	-171	15S32W	55	-58	-172	15S31W	56	-59	174	12S 4W	54(68)
3	43	-136	11N17E	48	43	-136	11N16E	47	46	-129	4N22W	52(80)
4	-6	9	20N35E	70	-6	9	20N35E	69	-2	11	7N36E	43(50)
5	24	-21	2N50E	49	24	-21	2N42E	49	20	-17	1N15E	31
6	17	-24	10S53E	44	17	-24	10S52E	44	16	-20	3N84W	40
7	-3	178	3S84W	56(60)	-2	177	3S55W	54(58)	-1	169	3N84W	52(55)
8	35	-133	6N24E	54	35	-133	5N25E	58	36	-126	4N71W	53
9	-25	33	11N63E	44	-25	33	10N65E	46	-15	26	13S74E	53
10	-11	15	14N52E	86(93)	-11	15	13N51E	88	-5	21	3S73E	71
11	-6	24	13N41E	43	-6	24	13N42E	41	-2	26	10N51E	38
12	-51	142	5N62E	60	-51	142	5N62E	63	-36	158	5S 2E	57(109)
13	-24	-128	8S55W	57	-24	-127	10S73W	51(52)	-23	-114	6S64W	37(54)
14	54	-12	14S49E	69	54	-12	14S49E	67	46	-10	9N85E	45
15	15	-20	7S59E	74	14	-20	15N86E	71	10	-15	14S88E	78
16	-10	-105	23S74W	75	-10	-104	28S73W	78	-11	-104	12S73W	62(69)
17	27	-122	13S64E	60	27	-122	13S64E	60	24	-117	4S22E	57
18	6	-152	9S39E	44(50)	7	-152	13S36E	51	7	-150	4S12W	37(51)
19	21	-2	18N78E	38	21	-2	18N78E	42	17	-1	23N45E	42(75)
20	60	-22	6S55W	19(31)	60	-22	6S50W	19(30)	61	-19	6S43W	19(39)
21	58	-23	15S25W	59	59	-23	18S33W	61	64	-16	29S17W	74
22	-31	-94	15S88E	57(63)	-31	-94	15S89E	57(63)	-31	-97	17S85E	57(62)
23	-40	50	11S37E	62	-40	50	9S41E	60	-36	42	10S37E	61
24	-33	-169	12S87W	58(62)	-33	-169	12S86W	57(63)	-29	167	7S48E	52
25	-44	-158	2N62E	78	-44	-157	6N52W	74	-31	-140	5S78E	55
26	-25	-155	8N86E	37(58)	-25	-153	5N89E	37(38)	-22	-141	6N79E	32(39)
27	-35	29	7S 0W	63	-36	29	5S 1E	61	-31	24	15N59W	94
28	-13	-140	11N17E	10(38)	-13	-140	11N17E	11(38)	-12	-138	15N45W	22(38)
29	-39	16	4S79W	67	-39	16	3S84W	66	-35	16	1S67W	68
30	23	-23	2N72W	62	23	-23	0S85W	62	19	-18	4S53W	70
31	-26	-130	13N38E	21(48)	-26	-130	13N38E	20(48)	-25	-129	9N44W	18(41)
32	34	-118	33S88E	73	34	-118	33S88E	73	35	-112	15S76E	41
33	-30	44	7S83E	36(62)	-30	44	6S76E	37(62)	-24	35	9S71E	48(62)
34	-17	9	9S63W	66	-17	8	9S61W	65	-10	2	7S34W	62
35	-17	-163	28N58W	48(54)	-17	-163	27N58W	47(53)	-16	-164	18N59W	47(57)
36	-24	-95	21N89E	66	-24	-95	21N89E	66	-27	-96	17N78E	52(60)
37	18	-117	10S37E	52	18	-117	10S36E	52	16	-115	3S20E	57
38	-18	-148	14N55W	3(34)	-18	-148	14N55W	9(34)	-18	-146	28N67W	20(31)
39	-46	-169	10N63W	61	-46	-169	10N62W	61	-35	166	6S 4E	52
40	0	11	9N40E	65(76)	0	11	8N38E	65(76)	2	16	7N21E	63
41	-18	-8	8S65W	64	-18	-9	7S64W	64	-12	-14	6S 6E	43(69)
42	-34	11	1N43E	48	-34	10	4N65E	51	-31	13	3S68W	48(49)
43	-32	12	5N77W	65	-32	12	5N76W	66	-31	14	6N77W	58
44	41	-120	30N88E	60	41	-120	30N88E	60	42	-115	14S86E	31

It is assumed that the hotspots arise at the top of D". Hotspot motion $\bar{v}$ is averaged over the past 40 Myr or the entire lifetime of the plume (whichever is longer). Magnitudes are given in mm/yr, directions are given in °E/°W of S/N, e.g., 5S25E means motion with 5 mm/yr toward 25° east of south, i.e., SSE. Tilts are considered during the entire lifetime of the plume, but only at depths where they can lead to extinction within $\lesssim$ 100 Myr according to Figure 1. If the maximum tilt of the entire conduit is larger, it follows in parentheses. The hotspot number is given as in Table 1.

yields a hotspot surface motion that is, after an initial phase, equal to flow at the source depth. Since surface motion represents flow in similar depth regions for both source models A and B, calculated motions are, in fact, often similar in direction and magnitude in both cases. A detailed comparison is, however, beyond the scope of this paper.

Some noteworthy results for individual hotspots are a southward motion for Hawaii, Kerguelen, and (to a lesser extent, and only for mantle models 1 and 2) Marion and no strong latitudinal motion for Reunion. This is in accordance with results from paleomagnetism [*Sager and Bleil*, 1987; *Tarduno and Cottrell*, 1997; *Inokuchi and Heider*, 1992; *Torsvik et al.*, 1998] and

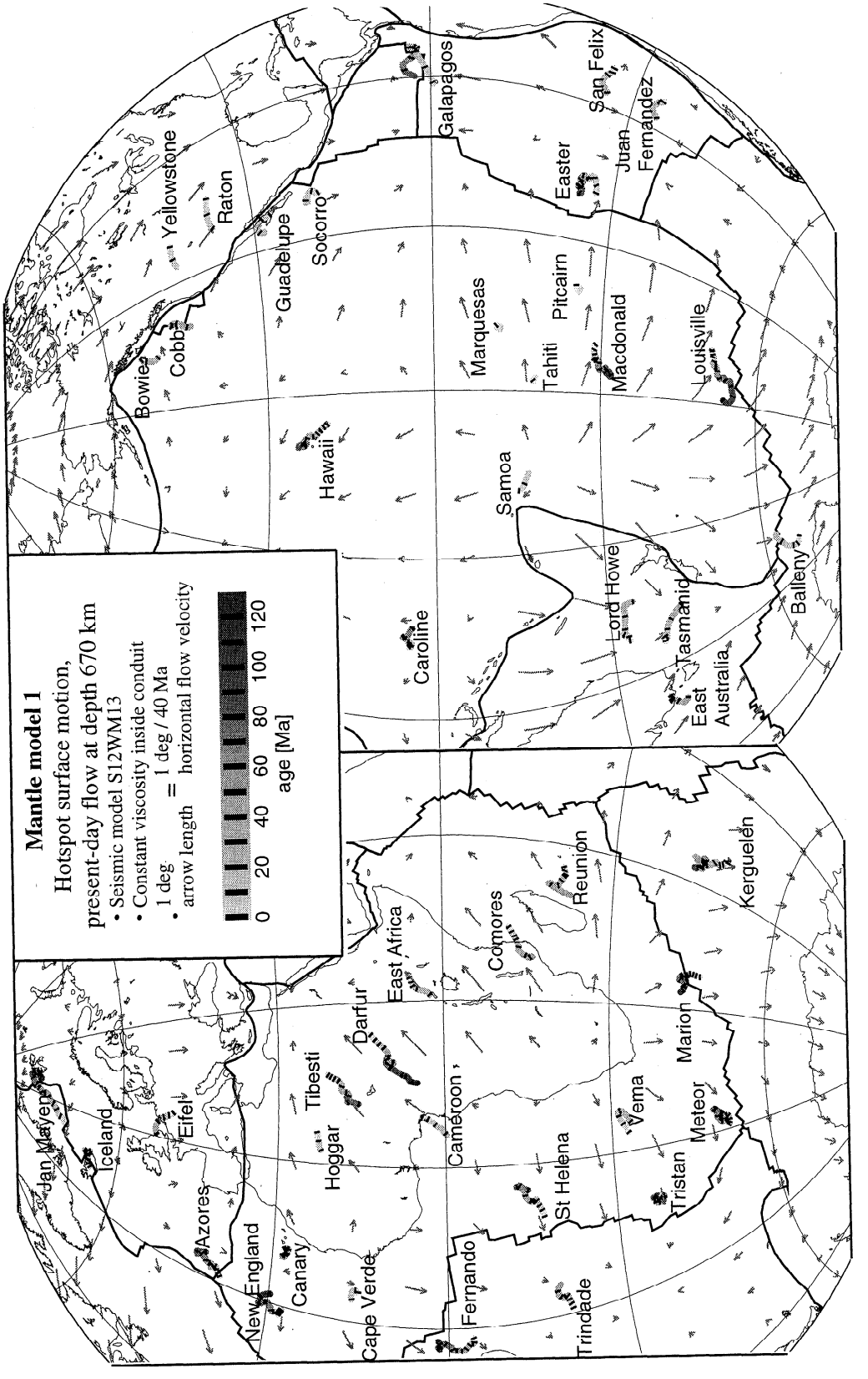

Figure 5. Hotspot surface motion and present-day flow at depth 670 km for mantle model 1.

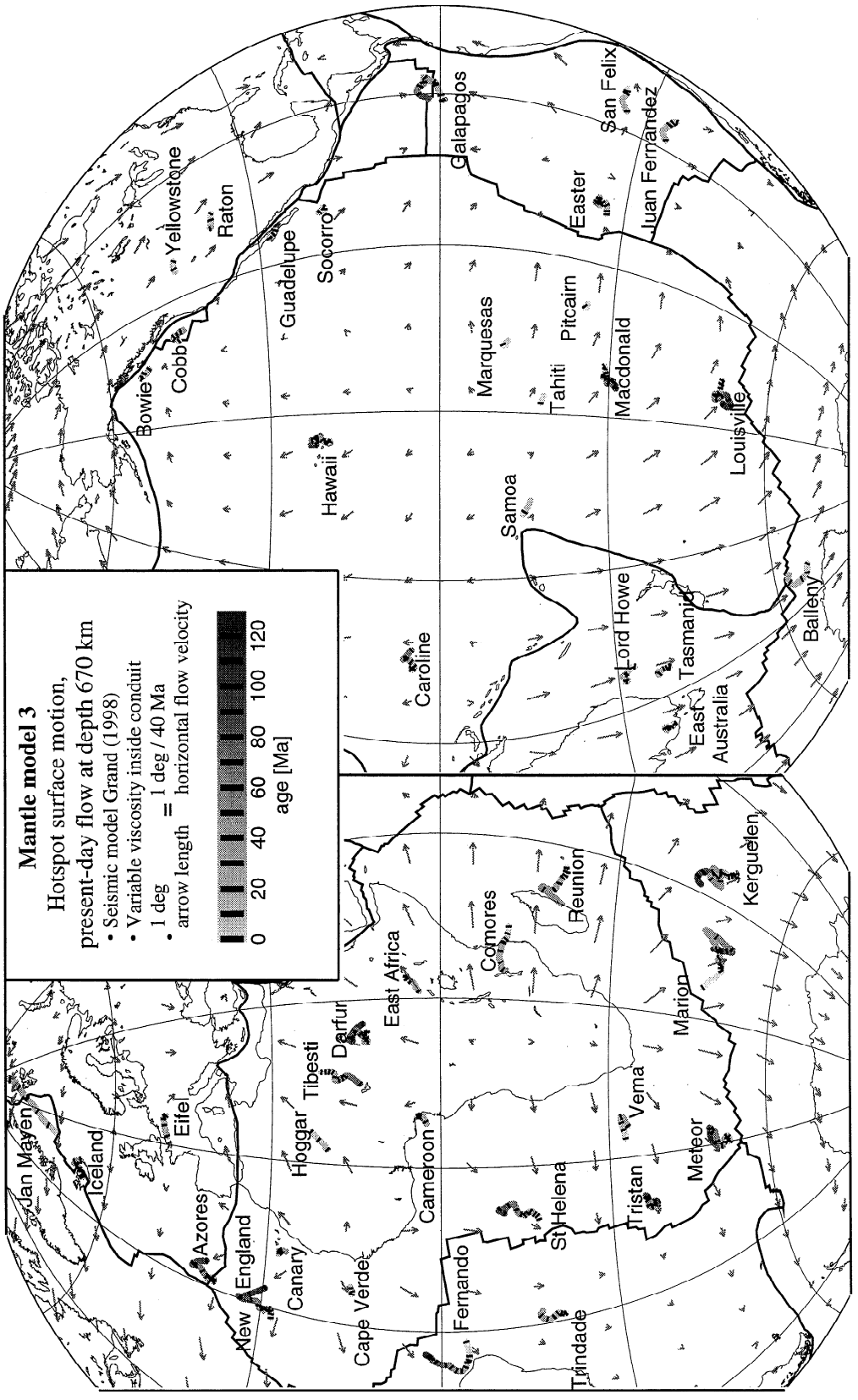

Figure 6. Hotspot surface motion and present-day flow at depth 670 km for mantle model 3.

will be discussed in a future paper. For hotspots on the African continent, results indicate a motion generally toward the northeast, in the direction of plate motion. This may be responsible for the Darfur hotspot being stationary relative to the plate for the past ≈ 40 Myr [*Franz et al.,* 1994] and for older volcanics toward the southwest of the currently active Cameroon Mountain [*Lee et al.,* 1994; *O'Connor and le Roex,* 1992], opposite to the age progression expected for a fixed hotspot. It can also help to explain the shift of volcanic activity from the flood basalts of the Ethiopian highlands toward recent activity in the Afar, but the calculated magnitude of motion is not sufficient to fully account for this movement. However, volcanism in both Cameroon and East Africa might not be due to plumes at all but rather may be related to continental rifting and more large-scale mantle upwellings. All three mantle models show a westward motion of the Iceland hotspot. In combination with the somewhat different models of absolute plate motion, a hotspot location is predicted that is closer than the present location to where rifting of the North Atlantic started about 60 Myr ago. For the Fernando hotspot the predicted location of the plume head at 201 Ma (not shown in the figures because only motion during the past 130 Myr is plotted) is between 500 and 1000 km toward the northnortheast of Fernando for all the three mantle models. The Fernando hotspot has been associated with the "Newark" plume head causing flood basalts at the triple junction of the North American, South American, and African plate prior to rifting of the Atlantic [*Leitch et al.,* 1998]. More results for individual hotspots are given in section 5, where some representative hotspot tracks are discussed.

5. Hotspot Tracks on Plates

5.1. Calculation of Hotspot Tracks

Figures 5 and 6 show the locations where, according to the calculations, hotspots were located at given times in a common mantle reference frame. However, any volcanic edifices produced at that place and time would have been moved to a different present location due to plate motions. For given time-dependent plate motions these present locations, which define the "hotspot tracks," can be calculated using rotation matrices as described in the appendix, following *Chang et al.* [1990].

5.1.1. Models of relative and absolute plate motions. Relative plate motions were adopted from *Müller et al.* [1993] for the African, South and North American, Australian, Indian, and Antarctic plates for 0–130 Ma, from *Gordon and Jurdy* [1986] for 0–64 Ma, and from *Lithgow-Bertelloni and Richards* [1998] for 64–120 Ma for other plates. Since earlier tabulated plate motions were unavailable, plate motion data for the earliest available time interval were also used before that. No tracks are plotted before 130 Ma. Therefore earlier plate motions only entered the calculations for the few hotspots assumed older than 130 Ma as boundary conditions for the flow.

Using geometry and age data from hotspot tracks, these plate motions were subsequently incorporated into an absolute reference frame. The calculated hotspot motions were also considered here, whereas in previous publications, hotspot fixity had been assumed. Using the method outlined in the appendix, motions of the Pacific plate were redetermined for the last 80 Myr, and of the African plate for the last 68.5 Myr; in this way, the calculated motion of the hotspots that were chosen to redetermine plate motions also determines the calculated tracks of other hotspots. The method requires at least two hotspot tracks for each independently determined plate motion. On the African plate, Tristan and Reunion were chosen since they both are associated with flood basalts that allow an age estimate, both have well-defined hotspot tracks with sufficient age data, both have historic volcanism that may be used to estimate their present position, and the anomalous mass flux could be determined for both with either good or fair reliability [*Sleep,* 1990]. The section of the Reunion track on the Indian plate was also used. Subsequently, African plate motion for the last 20.5 Myr was redetermined using St. Helena instead of Tristan, since chains of individual seamounts appear more suitable than more massive hotspot tracks to determine absolute plate motion [*O'Connor et al.,* 1999]. The results were then combined; the plate rotation between 20.5 and 42.7 Ma was adjusted such that the finite rotation for 42.7 Ma does not change. On the Pacific plate, Hawaii and Louisville were chosen, since they are the only hotspot chains on the Pacific plate with well-defined, narrow topographic features and a clear age progression that spans the entire Cenocoic. Age data were adopted from *Clague and Dalrymple* [1989], *Tarduno and Cottrell* [1997], and *Watts et al.* [1988]. Subsequently, Pacific plate motion for the last 5 Myr was also redetermined using Hawaii and Tahiti because sufficient data showing a clear age progression are available for both. For Tahiti, plume source model B was used because this model can give a better fit to the observed age progression (see below); for all other plumes, source model A was used. Pacific and African plate motions were hence independently determined. As discussed by *Gordon and Jurdy* [1986], this approach requires an additional plate boundary between East and West Antarctica or in the South Pacific. The implications of hotspot motion on relative motion along such a boundary and on mean lithospheric rotation will be discussed in detail in a future paper. The resulting plate motions are listed in Table 3. In all cases, Pacific plate motion substantially speeds up at 25 Ma, as has been previously proposed by *Lonsdale* [1988] and slightly changes direction at 5 Ma, as noted by *Wessel and Kroenke* [1997]. The magnitude of Pacific plate motion in mantle models 1–3 (moving hotspots) tends to be less than in mantle model 0 (fixed hotspots) because

Table 3. "Absolute" African and Pacific Plate Rotations in a Mean Mantle Reference Frame.

	Mantle Model 0			Mantle Model 1			Mantle Model 2			Mantle Model 3		
t, Myr	Lat	Long	Mag	Lat	Long	Mag	Lat	Long	Mag	Lat	Long	Mag
					African							
0.0–20.5	—	—	—	53	-36	0.19	55	-39	0.19	64	-55	0.21
20.5–42.7	—	—	—	39	-59	0.34	40	-58	0.35	36	-54	0.29
42.7–68.5	—	—	—	9	-41	0.22	10	-42	0.23	26	-58	0.19
					Pacific							
0.0– 5.0	-64	99	1.00	-64	105	0.93	-64	102	0.92	-65	92	1.00
5.0–25.0	-73	122	0.87	-75	94	0.86	-75	81	0.89	-74	130	0.86
25.0–43.0	-59	122	0.58	-54	151	0.54	-56	146	0.54	-58	150	0.57
43.0–68.0	-8	105	0.59	-1	103	0.58	-1	98	0.60	-7	103	0.56

These were re-determined for the time intervals for fixed hotspots (model 0) and three models of moving hotspots, using the method described in the appendix. For each time interval a constant rotation rate vector is assumed. Vectors are given in spherical coordinates (lat, latitude(deg); long, longitude(deg); and mag, magnitude(deg/Myr)). Absolute rotation of the African plate for the fixed hotspots model or before 68.5 Ma was not redetermined but was adopted from *Müller et al.* [1993].

calculations yield hotspot motion in a direction roughly opposite to plate motion. However, for the choice of parameters adopted in this paper this effect is rather small compared to other reasonable models [*Steinberger and O'Connell,* 2000]. All three mantle models still require a substantial change in Pacific plate motion at 43 Ma. They do not support the hypothesis proposed by *Norton* [1995] that the bend in the Hawaiian-Emperor chain is solely due to hotspot motion.

5.1.2. Hotspot track(s): On which plate? In order to calculate hotspot tracks on plates, one also needs to know on which plate a hotspot is located at any given time. This is possible in principle for given sets of plate rotations and boundaries. The plate models that are presently available in a usable format [*Lithgow-Bertelloni and Richards,* 1998] use constant plate boundaries for given (and rather long) time intervals. In reality, for example, geometric constraints require ridges to move continuously if spreading is symmetric and the plates on either side do not move at the same speed. Some of the boundary jumps between time intervals in the plate model may therefore at least partly be artifacts. These jumps can lead to corresponding kinks in the calculated hotspot tracks. An example is shown in Figure 7, where parts of the track that have initially been on the South American plate have been transferred to the African plate owing to ridge jumps according to the plate model.

Since it is not obvious which jumps correspond to real ridge jumps and which ones are introduced by the parameterization of the plate model, the solid tracks plotted in Figure 8 to 14 were generally calculated somewhat differently. If a hotspot is under, or close to, a given plate at a given time, the motion of that plate was applied for all following times in order to calculate a corresponding present location of volcanics produced by the hotspot. This means that, in general, it was assumed that fragments of one plate cannot change to another plate, i.e., plate boundaries do not change discontinuously. Obviously, this did not permit accurate treatment in some cases: For example, part of the Easter track that is now on the Nazca plate may have initially been produced on the Pacific plate and subsequently been transferred to the Nazca plate by a ridge jump; bathymetry maps show features along the Sala y Gomez/Nazca ridges that resemble such kinks and may be associated with ridge jumps.

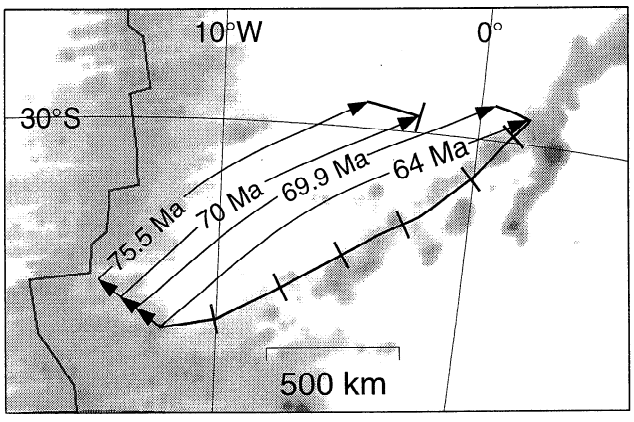

Figure 7. Track on African plate produced by a fixed hotspot at the location of Tristan da Cunha, calculated by taking the plate boundary reconstructions literally. For illustration the approximate paths that rocks have taken from the hotspot to their present location are also sketched in. Times at which rocks were produced are indicated along the paths. Elevations above -1000 m are shown shaded.

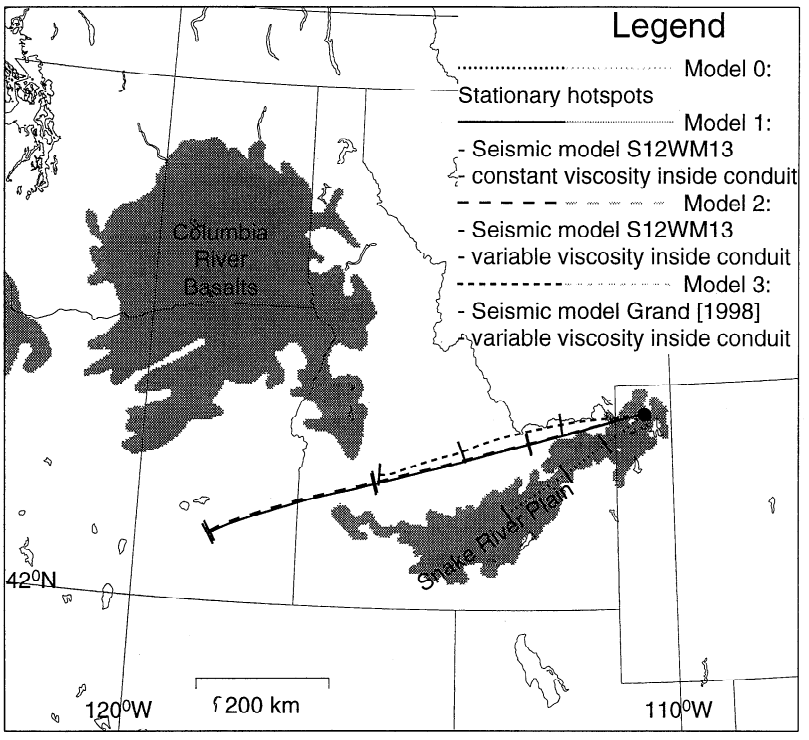

Figure 8. Yellowstone hotspot track. The Snake River Plain (distribution of quarternary and presumed quarternary volcanism) is drawn according to *Suppe et al.* [1975], and distribution of the Columbia River Basalts is drawn according to *Press and Siever* [1990]. Tick mark interval is 5 Myr.

On the basis of the observation that a hotspot, such as Tristan, may leave tracks on more than one plate at the same time, it is not required for the hotspot to be exactly under the plate. This is implemented by plotting a solid track if either the hotspot position itself or any of the corners of a regular hexagon surrounding the hotspot at a distance of 200 km is on that plate at the corresponding time.

If a hotspot is not under, or close to, a given plate at a given time, the rotation of that plate for all following times may still be used in order to calculate a corresponding present location. These locations are plotted as a grey "ghost" track on that plate. A grey track may correspond to an actual hotspot track, e.g., if the model plate boundary was chosen at the wrong location.

5.2. Results of Hotspot Tracks

Figures 8 to 14 show maps and age-distance plots for the calculated hotspot tracks, using either the calculated motion of hotspots (mantle models 1–3) or assuming hotspot fixity (mantle model 0). Results are compared with published age data, the distribution of igneous rocks (mostly volcanics) on continents, and ocean floor topography as compiled in the ETOPO5 data set [*National Geophysical Data Center,* 1988]. All these

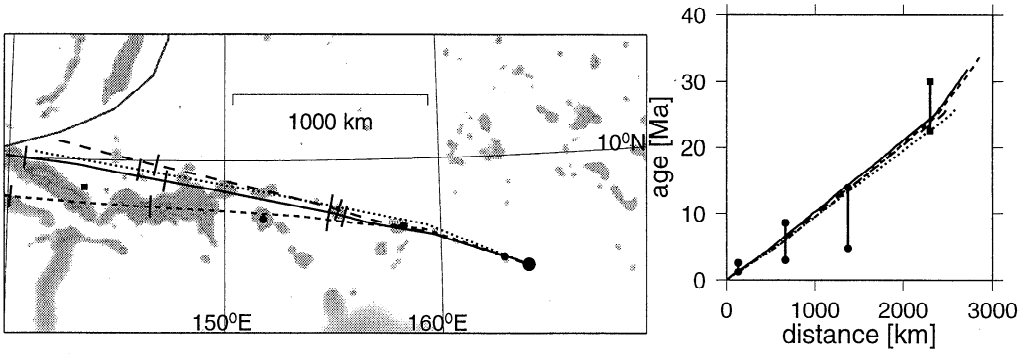

Figure 9. Caroline hotspot track. Age data are compiled by *Duncan and Clague* [1985] (circles) and *Jarrard and Clague* [1977] (square). Elevations above -3000 m are shown in variable shading; above -2000 m in dark shading. Tick mark interval is 10 Myr; for legend, see Figure 8.

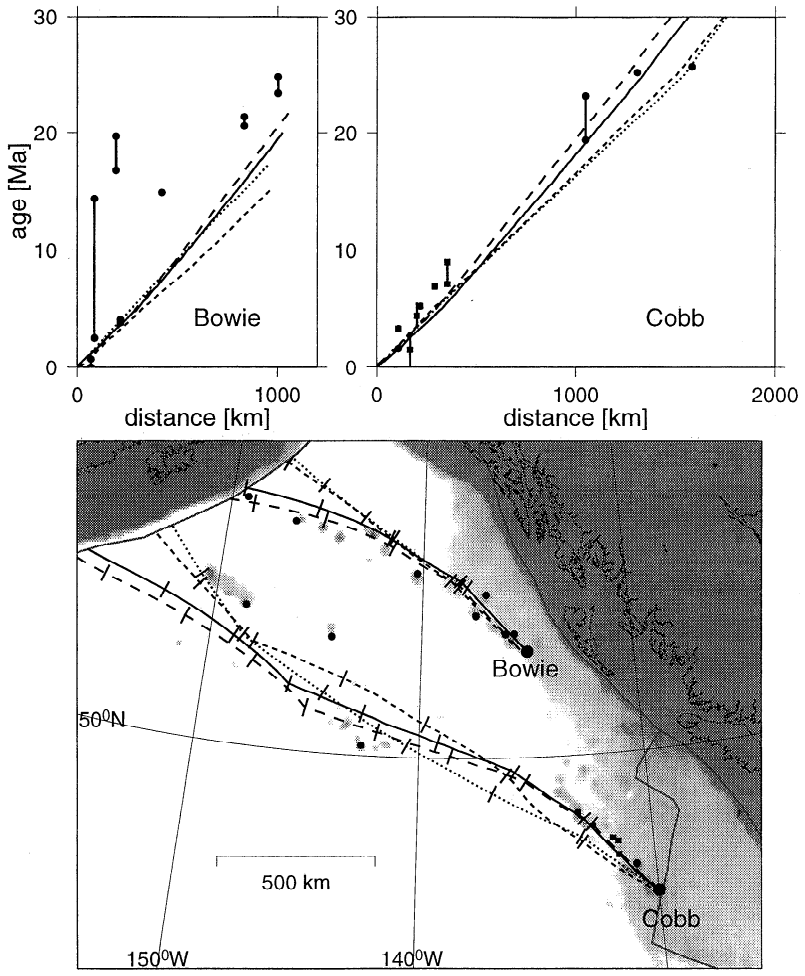

Figure 10. Bowie and Cobb hotspot tracks on the Pacific plate. Age data are compiled by *Duncan and Clague* [1985] (circles) and from *Desonie and Duncan* [1990] (squares). Elevations above -3200 m are shown in variable shading, above -2000 m in dark shading. Tick mark interval is 5 Myr; for legend, see Figure 8.

maps have 10° grid spacing. Assumed hotspot locations are shown as large solid dots. Where illustrative, plate boundaries and/or locations of dated samples are included in the maps. The same symbols are used in maps and x-t diagrams for corresponding data points.

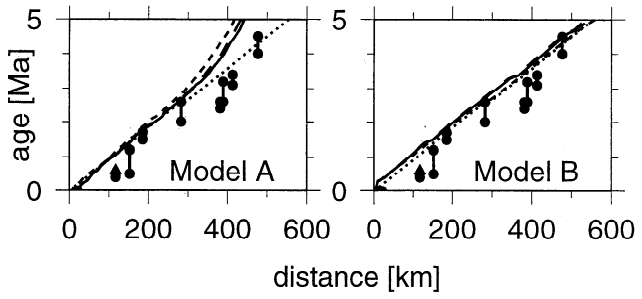

Figure 11. Age progression for Tahiti, source models A and B. Age data are compiled by *Duncan and Clague* [1985] (circles), and *Epp* [1984] (triangle). For legend, see Figure 8.

5.2.1. Results for Pacific hemisphere. Since the motions of the Louisville and Hawaiian hotspots are used to redetermine Pacific plate motion and their computed relative motion is small and in accordance with the observed hotspot tracks, mantle models 1–3 can fit the observed tracks just as well as the fixed hotspot model. Since the models predict a westward motion of the Easter hotspot and Nazca plate motion tends to be faster in the models including hotspot motion, the fit to the age progression of the Easter chain [*O'Connor et al.*, 1995] is better for mantle models 1–3 than for model 0. Results for these three hotspots are given by *Steinberger and O'Connell* [2000] and are not shown here. Hence the Yellowstone, Caroline, Bowie, and Cobb hotspot tracks have been chosen as illustrative examples.

The Yellowstone hotspot track is shown in Figure 8. Ages of volcanism in the Snake River Plain generally shift from the earliest (mid-Miocene, i.e., ~15 Ma) in the west to recent activity on the Yellowstone Plateau, according to *Wood and Kienle* [1990]. Quarternary volcanism along the entire Snake River Plain may indicate

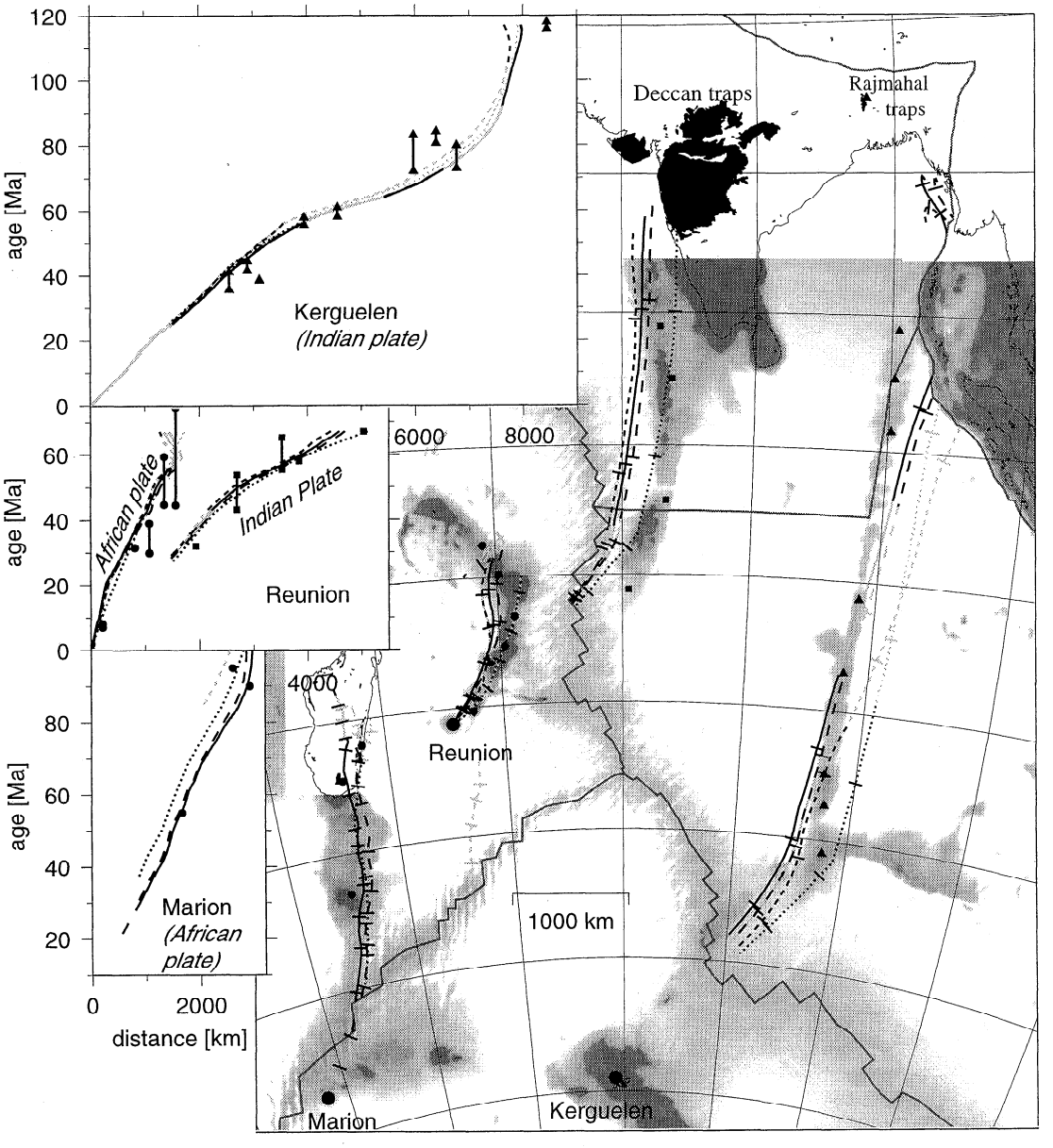

Figure 12. Hotspot tracks in the Indian Ocean. Age data for Kerguelen track are from *Duncan* [1978], *Duncan* [1991], *Müller et al.* [1993], and *Morgan* [1981], for Reunion track from *Duncan and Hargraves* [1990, and reference herein] and compiled by *Müller et al.* [1993], for Marion track from *Duncan* [1981] and *Duncan and Richards* [1991]. For a region in India the distribution of Tertiary extrusives (Deccan Traps) and Lower and Middle Jurassic extrusives (Rajmahal Traps), for Madagascar the distribution of Cretaceous extrusives is shown solid according to *Choubert and Faure-Muret* [1976]. In other areas, elevations above -4000 m are shown in variable shading, above -1000 m in dark shading. For clarity, the calculated Kerguelen track is only shown on the Indo-Australian plate the Marion track only on the African plate. In order to calculate the tracks on the Indo-Australian plate the Indian plate motion relative to Africa is used. Using the motion of the Central Indian Basin also listed by *Müller et al.* [1993] leads to very similar results. Tick mark interval is 10 Myr; for legend, see Figure 8.

continuing volcanic activity long after the hotspot has passed. The Columbia River Basalts are, however, offset from a track following the Snake River Plain. The calculations yield a predominantly eastward flow in the upper mantle which is reflected in the hotspot motion. Therefore the models with moving hotspots help to explain the observed ages (especially mantle model 3) and bring the track closer to the Columbia River Basalts. A better agreement of the predicted tracks with the observed distribution of volcanics would, however, require a rather fast southward flow (~10 cm/yr) in the asthenosphere.

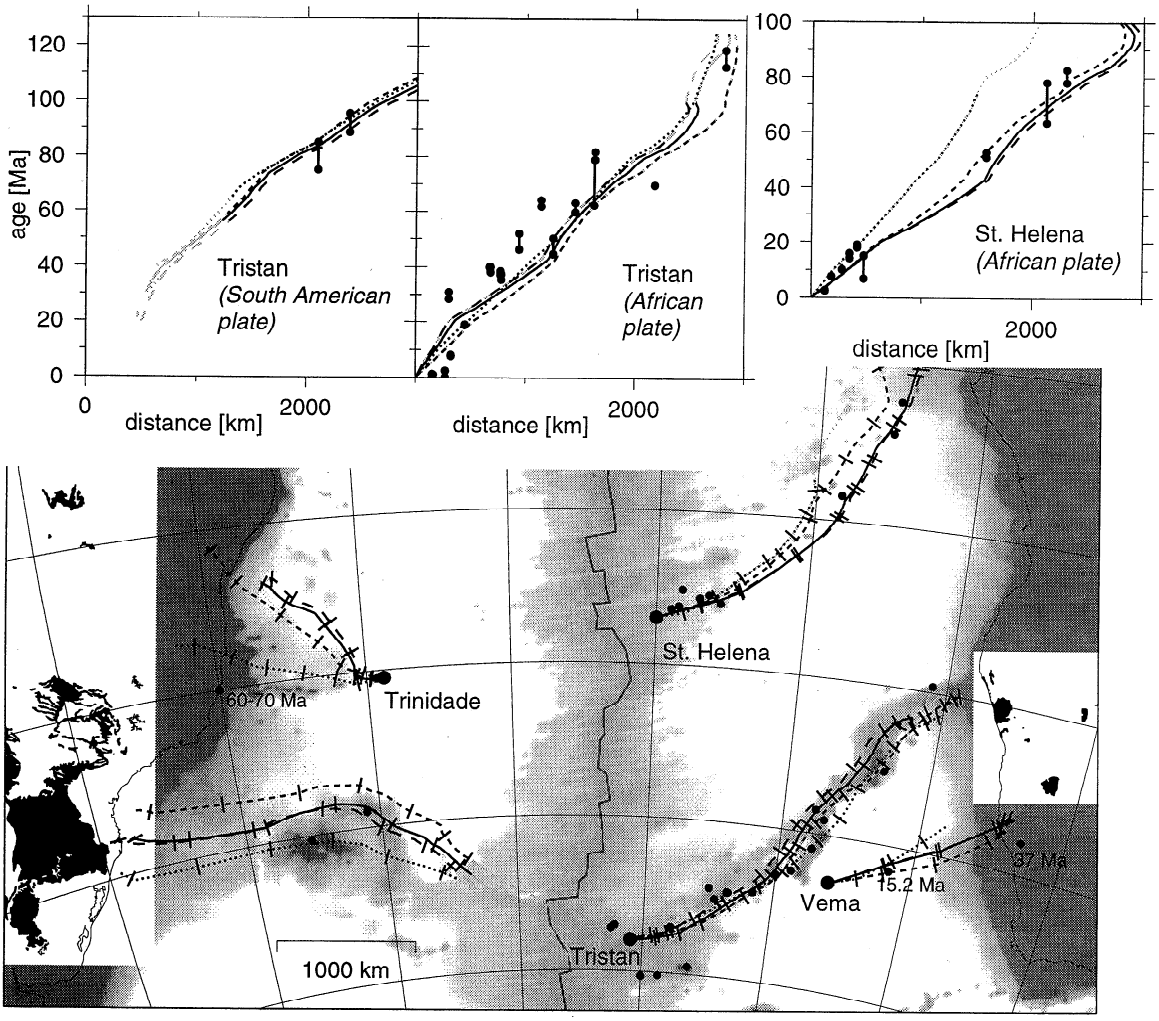

Figure 13. Hotspot tracks in the South Atlantic. Age data for Tristan track are from *O'Connor and Duncan* [1990] and *O'Connor and le Roex* [1992]; for St. Helena track from *Duncan* [1981], *O'Connor and le Roex* [1992], and *O'Connor et al.* [1999]; for Trindade track from *Morgan* [1981]; for Vema track from *O'Connor and le Roex* [1992] and *Morgan* [1981]. For a region in South America the distribution of Cretaceous and Jurassic basic volcanics including Parana flood basalts, for a region in Africa the distribution of Jurassic volcanics including Etendeka flood basalts is shown solid according to *Choubert and Faure-Muret* [1976]. In other areas, elevations above -4500 m are shown in variable shading, above -1500 m in dark shading. For clarity, the St. Helena track is only shown on the African plate. Tick mark interval is 10 Myr; for legend, see Figure 8.

Figure 9 shows that for the Caroline hotspot all mantle models give a good fit with observed seamount and island locations and ages.

The ages of Bowie and Cobb hotspots (Figure 10) are unknown because the tracks end at a subduction zone. For both hotspots a rather young age is assumed. For an older age, conduits would have been advected into the downwelling flow associated with subduction and hence would have been strongly distorted, according to the calculations. The hotspots would therefore not have survived to the present. Also, the strong tilt would cause a fast hotspot motion just as shown for the Galapagos hotspot in Figure 5, and agreement with the observed tracks would deteriorate.

For the assumed young ages, models tend to predict a slight southward to southeastward motion after an initial phase of northward to northwestward motion, corresponding to a change of flow direction with depth. The tracks for moving hotspots thus tend to show a curvature toward the right (running from old to young ages). With some uncertainty, one can see such a curvature at least in the Bowie track. Mantle model 1 yields approximately the right amount of curvature. The age of 43 Ma assumed for Cobb is equal to the age of the bend in the Hawaiian-Emperor chain. A plume head rising at the NE boundary of the Pacific plate would exert a net force on the Pacific plate in approximately the same direction as the difference in plate motion be-

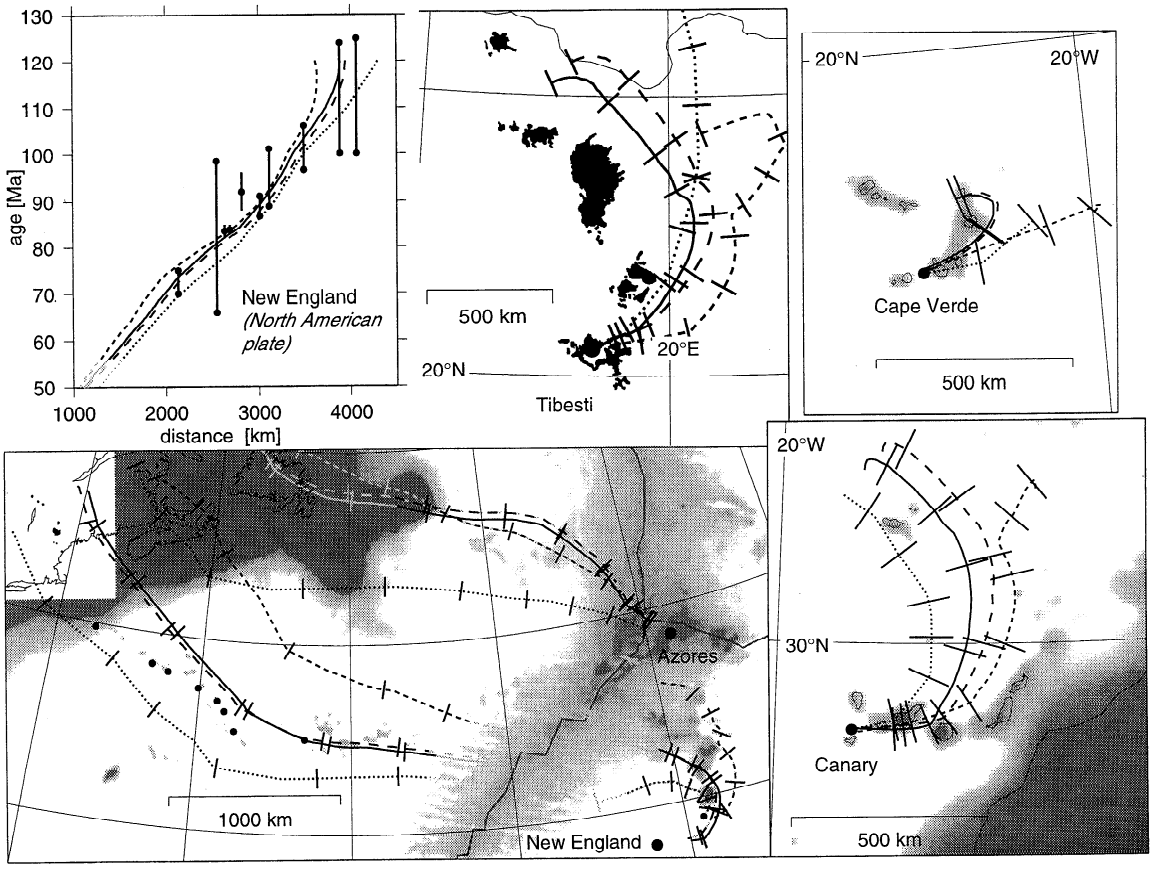

Figure 14. Hotspot tracks in the North Atlantic and North Africa. Age data for New England Seamounts are from *Duncan* [1984]. In a region of northern Africa (top middle panel) the distribution of Neogene volcanics and for a region in North America the distribution of Mesozoic granitic and syenitic intrusives including White Mountains and Monteregian Hills is shown as solid according to *Choubert and Faure-Muret* [1976]. In other areas of the bottom left map, elevations above -4000 m are shown in variable shading, above -1500 m in dark shading; in the maps for Canary and Cape Verde Islands, elevations above -2000 m are shown in variable shading, above sea level in dark shading. Tracks for New England hotspot are only shown until 15 Ma, approximately the age of Great Meteor Seamount [*Duncan,* 1984]. For the fixed hotspot case a different present location is chosen in order to match the location of Great Meteor Seamount (29°W, 29°N) at $\approx$ 15 Ma. For clarity, the Azores track is only shown on the North American plate. Tick mark interval is 10 Myr; for legend, see Figure 8.

fore and after the bend. However, no suitable physical mechanism for a sudden change in absolute plate motion without significant change of relative plate motions in the Pacific region has been proposed to date.

To illustrate the differences between source models A (deep origin) and B (shallow origin), age-distance plots are shown for Tahiti for both source models in Figure 11: Source model B can explain the observed more or less linear age progressions better: A plume starting with a vertical conduit would initially get advected in the same direction as plate motion; therefore the motion relative to the plate would be slower initially.

5.2.2. Results for African hemisphere. Figure 12 shows results for the Reunion, Kerguelen, and Marion hotspots. Although the Reunion hotspot track was also used to redetermine absolute plate motions, the calculated tracks for a moving hotspot on the Indian plate are to the west of Chagos-Maldives-Laccadives ridge. Apparently, the models (especially mantle model 3) predict too much eastward hotspot motion. The predicted Reunion track on the Indian plate ends right at the Carlsberg ridge, where it is therefore older than the ocean floor it is on. Such an unrealistic result can occur as the plate model has constant boundaries for long time intervals, whereas in reality the ridge migrates steadily. For a fixed Kerguelen hotspot a present location under the western Kerguelen plateau has to be assumed in order to achieve an acceptable fit of Ninetyeast Ridge [e.g., *Müller et al.*, 1993]. Here instead a present location at Kerguelen Island is assumed. In this case, mantle models 1 and 2 improve the fit of Ninetyeast ridge and Rajmahal traps compared to results from the fixed hotspots model. For mantle models 1 and 2 the hotspot is also located under or close to the Indian plate

(as required for leaving a track) for longer time periods, although still not permanently, as the rather continuous Ninetyeast ridge would suggest. A present hotspot location under Heard Island would be more plausible, given the volcanic activity; however, none of the mantle models gives an acceptable fit of Ninetyeast ridge and Rajmahal traps in this case. For the Marion hotspot, calculated and observed tracks fit well for the mantle models 0–2.

Figure 13 shows results for the Tristan, St. Helena, Vema, and Trindade hotspots. The present location of the Tristan hotspot was chosen between Tristan da Cunha and Gough Island because both have active or recent volcanism. For this location, all mantle models achieve good agreement with the Walvis ridge, which was used to redetermine absolute motion of the African plate. On the South American plate, all calculated tracks pass over, or just slightly north of Rio Grande Rise and begin near the Parana flood basalts. For the Vema hotspot the present location is not chosen at Vema Seamount (age 15 Ma according to *O'Connor and le Roex* [1992]) but at another seamount farther to the west. The predominantly westward hotspot motion calculated for the past 20 Myr, following the predominant midmantle flow direction in the region, can help to explain the only 22 Myr time difference between volcanism at Orange River [*Morgan,* 1981] and Vema Seamount. Similarly, for the St. Helena hotspot, the present location is not chosen at St. Helena island, but farther west, because volcanics on St. Helena are already 7–15 Ma old [*Duncan,* 1981]. Mantle models 1–3 predict hotspot motion toward the southeast, therefore a faster age progression along the track than the fixed hotspot model and therefore fit the age data better. They also approximately reproduce the observed trend of the seamount chain and for all times predict a hotspot location on or close to the African plate. This is in accordance with the observed seamounts but opposed to results from the fixed hotspot model. For the Trindade hotspot, mantle models 1–3 predict a southward to southwestward motion, thus deteriorating the fit with the observed submarine ridges when compared to using fixed hotspots. Results stay rather similar if a different age is assumed or source model B is used instead.

Figure 14 shows results for the New England, Azores, Cape Verde, Canary, and Tibesti hotspots. Great Meteor Seamount and the ridge toward the north of it, the New England and Corner seamounts, as well as igneous activity in the White Mountains and Monteregian hills have been associated with the "New England" hotspot, but alternative explanations have also been offered, as reviewed by *Duncan* [1984]. The mantle models 1–3 allow a better fit of the submarine ridge north of Great Meteor Seamount than the fixed hotspot model 0. On the North American plate the predicted track is south of the observed features when assuming a fixed hotspot but mostly north for the mantle models 1–3. The shift of the hotspot track resulting from the predicted hotspot motion is hence in the correct direction but somewhat too large. The situation is similar for Azores: a group of seamounts between Mid-Atlantic Ridge and Newfoundland might be part of the hotspot track. The fixed hotspot model predicts a track farther south and the mantle models 1–3 somewhat farther north. Results for Cape Verde are shown in order to illustrate the way in which the change in the horizontal mantle flow component with depth may lead to a change of hotspot motion in time. For mantle models 1 and 2 this yields a curvature of the track similar to the observed curvature of the island chain. These models start with an initially vertical conduit, but there is no evidence for a plume head/flood basalt that could have established it. For the Canary hotspot, calculated motion is very small, and the different tracks mostly represent different African plate motion models. Mantle models 1–3 predict a better agreement with the observed island chain than the fixed hotspot model. Among the widespread recent volcanism on the African continent, the field of Neogene volcanics from Tibesti toward the north most closely resembles a hotspot track. For mantle models 1 and 2 the calculated hotspot motion toward the northeast yields predicted tracks that match the observed distribution of volcanics better than assuming fixed hotspots. On the basis of the length of the track, an age of 80 Ma is assumed. However, all the volcanics have been mapped as Neogene (i.e., 0–24 Ma), which would require volcanism to continue for a very long time after the hotspot has passed.

6. Discussion and Outlook

The intention of this paper was to show that the observed geometry and age data of hotspot tracks do not require fixed hotspots but can also be explained by hotspots advected in mantle flow. The results show an improved fit as compared to assuming fixed hotspots in some cases, whereas in other cases the fit gets worse. Nevertheless, this model is more satisfactory than assuming fixed hotspots since it attempts (and in many cases successfully) to reconcile the observed hotspot tracks with the dynamics of the Earth's mantle. Owing to uncertainties and lack of detail in the model, no better agreement should be expected.

Figure 15 helps to assess more quantitatively the robustness of the results and its dependence on various model parameters. It shows that the main uncertainty comes from which mantle density model is chosen: Results are shown for density models derived from s and p wave tomographic models and subduction history, as well as an explicit low-resolution tomographic density model [*Ishii and Tromp,* 1999]. Figure 15, as well as comparison of Figures 3–6, and Table 2 show that in most cases, predicted directions of surface motion and tilt directions are similar for most density models. Mag-

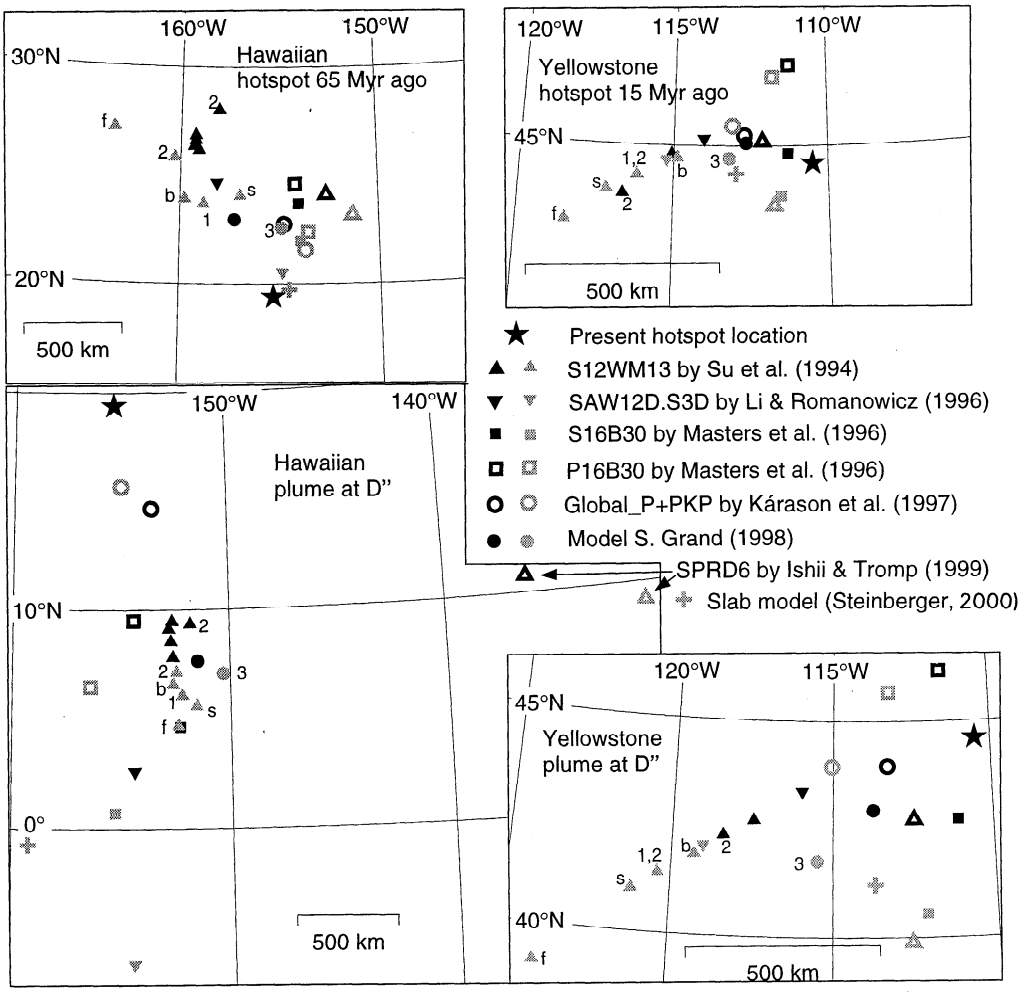

Figure 15. Summary of results for Hawaiian and Yellowstone hotspots for a greater number of mantle models. Calculated past hotspot surface locations and predicted locations of base of conduits are shown. Results are shown for the viscosity structure in Figure 1 (shaded symbols) and the preferred viscosity structure of *Steinberger and O'Connell* [1998, Figure 6], (solid symbols). For all shaded symbols in addition to mantle models 1–3 (marked with the corresponding numbers), buoyant rising speed is calculated with equation (3) and $u_0 = 2$ cm/yr. Solid symbols are calculated for an incompressible mantle without phase boundaries, and buoyant rising speed from (3) with $u_0 = 0.86$ cm/yr, except for solid triangles marked with "2", where equation (4) is used instead. In all cases except for Grand's model, $(\delta\rho/\rho) / (\delta v_s/v_s) = 0.2$ is assumed, and only wave speed anomalies below 220 km depth are considered. For the p wave models, $(\delta v_s/v_s) / (\delta v_p/v_p)$ values between 1.40 and 1.75 [*Calderwood,* 1999] are used. (left) Four solid triangles each for assumed hotspot ages 100, 110, 120, and 130 Ma. Symbols marked with the letters "b" (for big) and "s" (for small) were calculated with buoyant rising speed increased respectively reduced by 50%; letter "f" (for fast) means mantle density heterogeneities were increased by 50%. Density anomalies were advected for 68 Ma in all cases except for model SPRD6.

nitudes of surface motion and amount of tilt vary between different mantle models just as amplitudes vary between different density models.

Except for an initial effect that has been illustrated for the Bowie, Cobb, and Cape Verde hotspots, the assumed hotspot age tends to have little influence on the calculated surface motion as long as tilts stay reasonable. Obviously, the amount of tilt tends to increase with increasing age.

Predicted surface motion and the shape of plume conduits do not depend strongly on the assumed rising speed and its depth dependence. This can also be seen by comparison of mantle models 1 and 2 in Table 1. Dependence on the assumed viscosity structure is somewhat stronger. Results for the two viscosity structures compared in Figure 15 are still broadly similar. Any model that yields reasonable results will have a viscosity structure similar to these, and the results will also

be similar. In particular, lower mantle viscosity can not be decreased by any significant amount.

The fact that resulting hotspot motion stays roughly similar independent of assumed age, buoyancy flux, and viscosity structure is also evident from comparison with *Steinberger and O'Connell* [1998, Figures 7 and 8], who assumed equal age and buoyancy flux for all hotspots, and a different viscosity structure. Comparison with Figures 11 to 13 of *Steinberger and O'Connell* [1998], where the same buoyancy flux for all hotspots, a different viscosity structure, and (in Figure 11) the same age for all hotspots were assumed, again illustrates how the amount of tilt depends on assumed age, and that the predicted tilt, the shape of the plume conduit, and its location above D" do not depend much on detailed knowledge of plume rising speed and viscosity structure.

In some cases, e.g., East Africa, the apparent failure to achieve a satisfying fit suggests that volcanism might not be caused by a standard plume [*Whitehead and Luther,* 1975], but rather by a broader upwelling. If stress and deformation of the lithosphere due to large-scale mantle flow are also calculated, it will be possible to distinguish between hotspots and rifting caused by large-scale upwellings with greater confidence.

Because results of hotspot motion do not strongly depend on the assumed depth of origin (CMB or 670-km discontinuity being possible source depths), it is suggested that many of the plumes listed, particularly if the tracks do not originate at a flood basalt, or cover a rather short timespan, and/or the plumes are in regions of closely spaced volcanic activity (such as in the south central Pacific, eastern Australia or central Europe) may have an origin shallower than D". A more reliable distinction of source depth can probably be obtained in combination with geochemical characteristics observed for various hotspots [*Hofmann,* 1997]. For those hotspot originating in D", predicted source locations can be compared with seismic models of the lowermost mantle [*Kuo and Wu,* 1997].

In combination with models of true polar wander the models can predict paleolatitude changes of hotspots. On a recent Ocean Drilling Program (ODP) cruise, samples were collected on the Kerguelen plateau, and new paleolatitude results will soon be determined. It is hoped that future drilling missions can further increase the number of reliable paleolatitude data.

Appendix: A Least Squares Method for Determining Plate Motion From Hotspot Tracks

A method to find the "best fit" to hotspot tracks by a plate motion described by a small number of parameters is outlined. Specifically, in this paper only constant rotation rates in given time intervals are allowed for.

A1. Actual and Assumed Hotspot Locations

Assuming that plates are rigid, for all hotspots i on a plate, the positions $\tilde{\mathbf{y}}_i(\tilde{t})$ at time $\tilde{t}$ and the present positions $\tilde{\mathbf{x}}_i(\tilde{t})$ of the volcanics erupted at time $\tilde{t}$ at $\tilde{\mathbf{y}}_i(\tilde{t})$ are related by a single rotation matrix $\tilde{\mathbf{\Omega}}(\tilde{t})$:

$$\tilde{\mathbf{x}}_i(\tilde{t}) = \tilde{\mathbf{\Omega}}(\tilde{t}) \cdot \tilde{\mathbf{y}}_i(\tilde{t}). \tag{A1}$$

The rotation matrix can be fully described by three independent quantities as a function of time, e.g., by latitude and longitude of the rotation axis and the total rotation angle [*Chang et al.,* 1990].

The data on hotspot track i consist of measured ages t_{ij} $(1 < j < n_i)$ of rock samples collected at locations $\mathbf{x}_{ij}$ as well as the observed present location $\mathbf{x}_{i0}$. On the basis of $\mathbf{x}_{i0}$, past hotspot locations $\mathbf{y}_i(t_{ij})$ are inferred. However, the age determination of rocks involves some error, and the location of the hotspot may not exactly agree with the location at which volcanism occurs or a sample is found (hotspots have lateral extent; magma may not rise vertically through the crust).

Because of these errors, small intraplate deformations and uncertainties in the calculated hotspot motion, a rotation matrix $\mathbf{\Omega}(t)$, which is (apart from a few optional sharp bends) a smooth function of time and described by a small number of parameters (e.g., corresponding to constant rotation rates for two or three given time intervals) and satisfies

$$\mathbf{x}_{ij} = \mathbf{\Omega}(t_{ij}) \cdot \mathbf{y}_i(t_{ij}) \tag{A2}$$

cannot be found. However, a rotation matrix $\mathbf{\Omega}(t)$ with these properties, and vectors $\boldsymbol{\varepsilon}_{i0}$ and $\boldsymbol{\varepsilon}_{ij}$, which are parallel to the Earth's surface, as well as values Δt_{ij} such that

$$\mathbf{x}_{ij} + \boldsymbol{\varepsilon}_{ij} = \mathbf{\Omega}(t_{ij} + \Delta t_{ij}) \cdot (\mathbf{y}_i(t_{ij}) + \boldsymbol{\varepsilon}_{i0}) \tag{A3}$$

can be found.

A2. Minimizing Normalized Errors

In order to find a "best fitting" rotation matrix $\mathbf{\Omega}$ the errors in time and position measurement are estimated. The estimated error of the position x_{ij} can be described by an "error ellipse," which is defined by the angle φ_{ij} between the major half axis and the latitudinal direction, and the lengths of the major and the minor half axis, $\hat{\varepsilon}_{ij1}$ and $\hat{\varepsilon}_{ij2}$ (see Figure A1). Correspondingly, for the present time the error ellipse is defined by an angle φ_{i0} and half axes $\hat{\varepsilon}_{i01}$ and $\hat{\varepsilon}_{i02}$. The estimated errors in time shall be called $\Delta\hat{t}_{ij}$.

The deviation vectors $\boldsymbol{\varepsilon}_{i0}$ and $\boldsymbol{\varepsilon}_{ij}$ have components $\bar{\varepsilon}_{i01}$ or $\bar{\varepsilon}_{ij1}$ in the direction of the major half axis of the ellipsoid, and components $\bar{\varepsilon}_{i02}$ or $\bar{\varepsilon}_{ij2}$ in the direction of the minor half axis. By dividing the deviations in space and time by the corresponding estimated errors, "normalized" deviations

$$\breve{\varepsilon}_{i01} = \frac{\bar{\varepsilon}_{i01}}{\hat{\varepsilon}_{i01}} \qquad \breve{\varepsilon}_{i02} = \frac{\bar{\varepsilon}_{i02}}{\hat{\varepsilon}_{i02}} \tag{A4}$$

$$\breve{\varepsilon}_{ij1} = \frac{\bar{\varepsilon}_{ij1}}{\hat{\varepsilon}_{ij1}} \qquad \breve{\varepsilon}_{ij2} = \frac{\bar{\varepsilon}_{ij2}}{\hat{\varepsilon}_{ij2}} \qquad \Delta\breve{t}_{ij} = \frac{\Delta t_{ij}}{\Delta\hat{t}_{ij}}$$

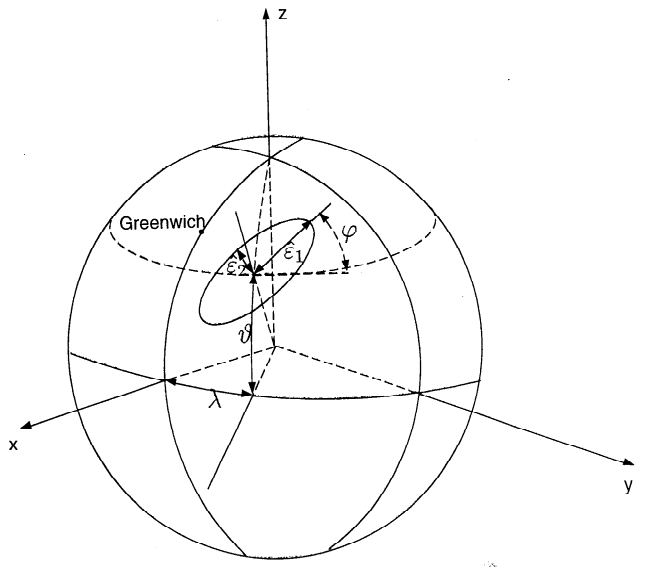

Figure A1. The ϑ_{ij} and λ_{ij} are latitude and longitude of hotspot i at time t_{ij}. The "error ellipse" is determined by the angle φ_{ij} between the major half axis and the latitudinal direction and the lengths of the major and the minor half axis $\hat{\varepsilon}_{ij1}$ and $\hat{\varepsilon}_{ij2}$. (Indices ij are omitted in the drawing.)

are obtained. The aim is to minimize the sum of squares of the normalized deviations,

$$\sum_i \left(\breve{\varepsilon}^2_{i01} + \breve{\varepsilon}^2_{i02}\right) + \sum_{i,j} \left(\breve{\varepsilon}^2_{ij1} + \breve{\varepsilon}^2_{ij2}\right) + \sum_{i,j} \Delta\breve{t}^2_{ij}. \quad \text{(A5)}$$

A3. Independent Parameters in the Sum of Squares

Only the normalized errors at time $t = 0$ and the parameters that determine the rotation matrix are independent parameters in (A5); $\breve{\varepsilon}_{ij1}$ and $\breve{\varepsilon}_{ij2}$ have to be expressed in terms of these. To do so, (A3) is written in Cartesian coordinates, with the x axis in the equatorial plane and at the longitude of Greenwich, the y axis in the equatorial plane and 90^0 east of Greenwich, and the z axis along the Earth's rotation axis:

$$\boldsymbol{\Omega}(t_{ij} + \Delta t_{ij}) \cdot \left[\begin{pmatrix} y_{i1}(t_{ij}) \\ y_{i2}(t_{ij}) \\ y_{i3}(t_{ij}) \end{pmatrix} + \begin{pmatrix} \varepsilon_{i01} \\ \varepsilon_{i02} \\ \varepsilon_{i03} \end{pmatrix} \right]$$
$$= \left[\begin{pmatrix} x_{ij1} \\ x_{ij2} \\ x_{ij3} \end{pmatrix} + \begin{pmatrix} \varepsilon_{ij1} \\ \varepsilon_{ij2} \\ \varepsilon_{ij3} \end{pmatrix} \right]. \quad \text{(A6)}$$

The ε_{i01}, ε_{i02} and ε_{i03} are now expressed by $\breve{\varepsilon}_{i01}$ and $\breve{\varepsilon}_{i02}$, and ε_{ij1}, ε_{ij2} and ε_{ij3} by $\breve{\varepsilon}_{ij1}$ and $\breve{\varepsilon}_{ij2}$, and the equation is solved for $\breve{\varepsilon}_{ij1}$ and $\breve{\varepsilon}_{ij2}$: After some algebra, this yields

$$\begin{pmatrix} \breve{\varepsilon}_{ij1} \\ \breve{\varepsilon}_{ij2} \end{pmatrix} = \mathbf{A}_{ij} \cdot \left\{ \boldsymbol{\Omega}(t_{ij} + \Delta t_{ij}) \cdot \left[\begin{pmatrix} y_{i1}(t_{ij}) \\ y_{i2}(t_{ij}) \\ y_{i3}(t_{ij}) \end{pmatrix} \right.\right.$$
$$\left.\left. + \mathbf{B}_i \cdot \begin{pmatrix} \breve{\varepsilon}_{i01} \\ \breve{\varepsilon}_{i02} \end{pmatrix} \right] - \begin{pmatrix} x_{ij1} \\ x_{ij2} \\ x_{ij3} \end{pmatrix} \right\}. \quad \text{(A7)}$$

The matrices $\mathbf{A}_{ij}$ have the components

$$\begin{aligned} A_{ij\,11} &= (-\sin\varphi_{ij} \sin\vartheta_{ij} \cos\lambda_{ij} - \cos\varphi_{ij} \sin\lambda_{ij}) / \hat{\varepsilon}_{ij1} \\ A_{ij\,12} &= (-\sin\varphi_{ij} \sin\vartheta_{ij} \sin\lambda_{ij} + \cos\varphi_{ij} \cos\lambda_{ij}) / \hat{\varepsilon}_{ij1} \\ A_{ij\,13} &= \sin\varphi_{ij} \cos\vartheta_{ij} / \hat{\varepsilon}_{ij1} \\ A_{ij\,21} &= (-\cos\varphi_{ij} \sin\vartheta_{ij} \cos\lambda_{ij} + \sin\varphi_{ij} \sin\lambda_{ij}) / \hat{\varepsilon}_{ij2} \\ A_{ij\,22} &= (-\cos\varphi_{ij} \sin\vartheta_{ij} \sin\lambda_{ij} - \sin\varphi_{ij} \cos\lambda_{ij}) / \hat{\varepsilon}_{ij2} \\ A_{ij\,23} &= \cos\varphi_{ij} \cos\vartheta_{ij} / \hat{\varepsilon}_{ij2}, \end{aligned} \quad \text{(A8)}$$

with ϑ_{ij} and λ_{ij} being latitude and longitude of $\mathbf{x}_{ij}$. Matrices $\mathbf{B}_i$ have the components

$$\begin{aligned} B_{i\,11} &= (-\sin\varphi_{i0} \sin\vartheta_{i0} \cos\lambda_{i0} - \cos\varphi_{i0} \sin\lambda_{i0}) \cdot \hat{\varepsilon}_{i01} \\ B_{i\,12} &= (-\cos\varphi_{i0} \sin\vartheta_{i0} \cos\lambda_{i0} + \sin\varphi_{i0} \sin\lambda_{i0}) \cdot \hat{\varepsilon}_{i02} \\ B_{i\,21} &= (-\sin\varphi_{i0} \sin\vartheta_{i0} \sin\lambda_{i0} + \cos\varphi_{i0} \cos\lambda_{i0}) \cdot \hat{\varepsilon}_{i01} \\ B_{i\,22} &= (-\cos\varphi_{i0} \sin\vartheta_{i0} \sin\lambda_{i0} - \sin\varphi_{i0} \cos\lambda_{i0}) \cdot \hat{\varepsilon}_{i02} \\ B_{i\,31} &= \sin\varphi_{i0} \cos\vartheta_{i0} \cdot \hat{\varepsilon}_{i01} \\ B_{i\,32} &= \cos\varphi_{i0} \cos\vartheta_{i0} \cdot \hat{\varepsilon}_{i02}, \end{aligned} \quad \text{(A9)}$$

with ϑ_{i0} and λ_{i0} being latitude and longitude of $\mathbf{x}_{i0}$. For visualization of the different quantities in these equations see Figure A1.

A4. Two-Step Approach to Minimize the Sum of Squares

If n is the number of hotspots, n_t is the number of data points for past times and N_p is the number of parameters on which the rotation matrix depends, a minimization in $2n + n_t + N_p$ dimensions has to be carried out, since there are $2n$ deviations of the present hotspot positions, n_t time errors, and N_p parameters to be determined. The $2n_t$ deviations of past hotspot positions are not independent variables but are determined by (A7). As an additional constraint, $\boldsymbol{\Omega}(0)$ has to be the identity matrix or, in practical terms, at least deviate very little from the identity matrix.

The number of dimensions can be decreased to $2n + N_p$ if we first do not consider any time errors. This means

$$\sum_i \left(\breve{\varepsilon}^2_{i01} + \breve{\varepsilon}^2_{i02}\right) + \sum_{i,j} \left(\breve{\varepsilon}^2_{ij1} + \breve{\varepsilon}^2_{ij2}\right) \quad \text{(A10)}$$

is minimized with the constraint

$$\begin{pmatrix} \breve{\varepsilon}_{ij1} \\ \breve{\varepsilon}_{ij2} \end{pmatrix} = \mathbf{A}_{ij} \cdot \left\{ \boldsymbol{\Omega}(t_{ij}) \left[\begin{pmatrix} y_{i1}(t_{ij}) \\ y_{i2}(t_{ij}) \\ y_{i3}(t_{ij}) \end{pmatrix} \right.\right.$$
$$\left.\left. + \mathbf{B}_i \cdot \begin{pmatrix} \breve{\varepsilon}_{i01} \\ \breve{\varepsilon}_{i02} \end{pmatrix} \right] - \begin{pmatrix} x_{ij1} \\ x_{ij2} \\ x_{ij3} \end{pmatrix} \right\}, \quad \text{(A11)}$$

and a first solution $\boldsymbol{\Omega}_1(t)$ is obtained. With this solution the time errors can now be converted into spatial errors: Times $t_{ij} + \Delta\hat{t}_{ij}$ and $t_{ij} - \Delta\hat{t}_{ij}$ correspond to positions $\mathbf{x}_{ij,+} = \boldsymbol{\Omega}_1(t_{ij} + \Delta\hat{t}_{ij}) \cdot (\mathbf{y}_i(t_{ij}) + \boldsymbol{\varepsilon}_{i0})$ and $\mathbf{x}_{ij,-} = \boldsymbol{\Omega}_1(t_{ij} - \Delta\hat{t}_{ij}) \cdot (\mathbf{y}_i(t_{ij}) + \boldsymbol{\varepsilon}_{i0})$. Here it is always assumed that in the first step the error ellipsoid is a circle with radius $\hat{\varepsilon}_{ij2}$. Then the new error ellipsoid will be have a major half axis

$$\hat{\varepsilon}_{ij1} = \sqrt{\hat{\varepsilon}_{ij2}^2 + \Delta_{ij}^2}, \text{ where } \Delta_{ij} \simeq \frac{1}{2}\|\mathbf{x}_{ij,+} - \mathbf{x}_{ij,-}\|,$$

and the direction of the major half axis is in the direction of $\mathbf{x}_{ij,+} - \mathbf{x}_{ij,-}$. With these new error estimates and the first solution as starting point, a second minimization is performed, and a new solution is found.

Like the "hotspotting" method described by *Wessel and Kroenke* [1997], this method neither requires radiometrically dated ages, nor explicit knowledge of the present hotspot location. The ages technically required as input can be chosen according to the location of the "data point" (e.g., seamount) along the track. However, in the second step the age error can be chosen to be sufficiently large such that the error ellipses become very elongated along the track. In this way, essentially the geometry of the track can be fit, the influence of the assumed ages on the result being rather small. The present location may initially be guessed, with a sufficiently large estimated error; the method then yields a best fitting present location.

A5. Explicit Expression of the Rotation Matrix

For a finite rotation of magnitude $\rho = \|\boldsymbol{\tau}\| = (\tau_1^2 + \tau_2^2 + \tau_3^2)^{1/2}$ radians around the axis $\boldsymbol{\tau}/\|\boldsymbol{\tau}\|$, the rotation matrix is

$$\boldsymbol{\Omega}(t) = \mathbf{I} + \frac{\sin\rho(t)}{\rho(t)}\mathbf{T}(t) + \frac{1-\cos\rho(t)}{\rho(t)^2}\mathbf{T}(t)^2, \quad \text{(A12)}$$

where

$$\mathbf{T} = \begin{pmatrix} 0 & -\tau_3 & \tau_2 \\ \tau_3 & 0 & -\tau_1 \\ -\tau_2 & \tau_1 & 0 \end{pmatrix}$$

and $\mathbf{I}$ is the identity matrix [*Chang et al.*, 1990]. A constant rotation rate $d\rho/dt$ around a constant axis in the time interval $[t_2, t_1]$ $(t_2 < t_1 < 0)$ corresponds to a total rotation of magnitude $d\rho/dt\,(t_1 - t_2)$ around the same axis. Thus in this case the rotation matrix $\boldsymbol{\Omega}_{12}$ representing the total rotation between times t_2 and t_1 can be calculated. If $\boldsymbol{\Omega}(t_1)$ and $\boldsymbol{\Omega}_{12}$ are known, $\boldsymbol{\Omega}(t_2)$ can be calculated by simple matrix multiplication:

$$\boldsymbol{\Omega}(t_2) = \boldsymbol{\Omega}(t_1) \cdot \boldsymbol{\Omega}_{12}. \quad \text{(A13)}$$

Hence rotation matrices can be calculated iteratively. Hotspot tracks on other plates may also be incorporated if relative plate rotations are known, as rotation rates can simply be added.

Acknowledgments. This work is based on research done with Rick O'Connell while the author was graduate student. A substantial part of this work was done during a postdoctoral fellowship at Academia Sinica (Taiwan). Some of the calculations were done by Maria Antretter. The least squares method is based on suggestions by Joann Stock and Jeff Love. Further contributions and suggestions by Ben-Yuan Kuo, Geoff Davies, Harro Schmeling, and Gabriele Marquart are appreciated. Comments by Paul Tackley and two anonymous reviewers helped to improve and shorten the manuscript. Michael James read the paper as a native speaker. Geoid kernels calculated with a code written by Svetlana Panasyuk helped to constrain the viscosity structure. Figures were prepared using GMT graphics [*Wessel and Smith*, 1995].

References

Akaogi, M., and E. Ito, Calorimetric study on majorite-perovskite transition in the system $Mg_4Si_4O_{12}$-$Mg_3Al_2Si_3O_{12}$: transition boundaries with positive pressure-temperature slopes, *Phys. Earth Planet. Inter., 114*, 129-140, 1999.

Akaogi, M., E. Ito, and A. Navrotsky, Olivine-modified spinel-spinel transitions in the system Mg_2SiO_4-Fe_2SiO_4: Calorimetric measurements, thermochemical calculations, and geophysical application, *J. Geophys. Res., 94*, 15,671-15,685, 1989.

Batchelor, G. K., *An Introduction to Fluid Mechanics*, Cambridge Univ. Press, New York, 1967.

Bijwaard, H., and W. Spakman, Tomographic evidence for a narrow whole mantle plume below Iceland, *Earth Planet. Sci. Lett., 166*, 121-126, 1999.

Burke, K., and J. T. Wilson, Hotspots on the Earth's surface, *Sci. Am., 235* (2), 46-57, 1976.

Calderwood, A. R., Mineral physics constraints on the chemical composition and temperature of the Earth's mantle, Ph.D. thesis, Univ. of B. C., Vancouver, 1999.

Campbell, I. H., and R. W. Griffiths, Implications of mantle plume structure for the evolution of flood basalts, *Earth Planet. Sci. Lett., 99*, 79-93, 1990.

Chang, T., J. Stock, and P. Molnar, The rotation group in plate tectonics and the representation of uncertainties of plate reconstructions, *Geophys. J. Int., 101*, 649-661, 1990.

Choubert, G., and A. Faure-Muret, *Atlas Geologique du Monde*, Commission de la Carte Geol. du Monde, UNESCO, Paris, 1976.

Clague, D. A., and G. B. Dalrymple, Tectonics, geochronology, and origin of the Hawaiian-Emperor volcanic chain, in *The Geology of North America*, vol. N, *The Eastern Pacific Ocean and Hawaii*, edited by E. L. Winterer, D. M. Hussong, and R. W. Decker, pp. 188-217, Geol. Soc. of Am., Boulder, Colo., 1989.

Davies, G. F., Ocean bathymetry and mantle convection, 1, Large-scale flow and hotspots, *J. Geophys. Res., 93*, 10,467-10,480, 1988.

Davies, G. F., Temporal variation of the Hawaiian plume flux, *Earth Planet. Sci. Lett., 113*, 277-286, 1992.

Desonie, D. L., and R. A. Duncan, The Cobb-Eickelberg seamount chain: Hotspot volcanism with mid-ocean ridge basalt affinity, *J. Geophys. Res., 95*, 12,697-12,711, 1990.

Duncan, R. A., Geochronology of basalts from the Ninetyeast Ridge and continental dispersion in the eastern Indian Ocean, *J. Volcanol. Geotherm. Res., 4*, 283-305, 1978.

Duncan, R. A., Hotspots in the southern oceans–An absolute frame of reference for motion of the Gondwana continents, *Tectonophysics, 74*, 29-42, 1981.

Duncan, R. A., Age progressive volcanism in the New England seamounts and the opening of the central Atlantic Ocean, *J. Geophys. Res., 89*, 9980-9990, 1984.

Duncan, R. A., Age distribution of volcanism along aseismic ridges in the eastern Indian Ocean, *Proc. Ocean Drill. Program Sci. Results, 121*, 507-517, 1991.

Duncan, R. A., and D. A. Clague, Pacific plate motion recorded by linear volcanic chains, in *The Ocean Basins and Margins*, vol. 7a, edited by A. E. M. Nairn, F. G. Stehli, and S. Uyeda, pp. 89-121, Plenum, New York, 1985.

Duncan, R. A., and R. B. Hargraves, $^{40}Ar/^{39}Ar$ geochronol-

ogy of basement rocks from the Mascarene Plateau, the Chagos Bank, and the Maldive Ridge, *Proc. Ocean Drill. Program Sci. Results, 115*, 43-51, 1990.

Duncan, R. A., and M. A. Richards, Hotspots, mantle plumes, flood basalts, and true polar wander, *Rev. Geophys., 29*, 31-50, 1991.

Duncan, R. A., N. Petersen, and R. B. Hargraves, Mantle plumes, movement of the European plate and polar wandering, *Nature, 239*, 82-86, 1972.

Dziewonski, A. M., and D. L. Anderson, Preliminary reference Earth model, *Phys. Earth Planet. Inter., 25*, 297-356, 1981.

Epp, D., Implications of volcano and swell heights for thinning of the lithosphere by hotspots, *J. Geophys. Res., 89*, 9991-9996, 1984.

Forte, A. M., A. M. Dziewonski, and R. L. Woodward, Aspherical structure of the mantle, tectonic plate motions, nonhydrostatic geoid, and topography of the core-mantle boundary, in *Dynamics of the Earth's Deep Interior and Earth Rotation, Geophys. Monogr. Ser.*, vol. 72, edited by J.-L. Le Mouël, D. E. Smylie, and T. Herring, pp. 135-166, AGU, Washington, D. C., 1993.

Franz, G., D. Pudlo, and K. Wemmer, The Darfur Dome, western Sahara: The product of a subcontinental mantel plume, *Geol. Rundsch., 83*, 614-623, 1994.

Garfunkel, Z., Darfur-Levant array of volcanics–A 140-Ma long record of a hotspot beneath the African-Arabian continent, and its bearing on Africa's absolute motion, *Isr. J. Earth Sci., 40*, 135-150, 1992.

Gordon, R. G., and D. Jurdy, Cenocoic global plate motions, *J. Geophys. Res., 91*, 12,389-12,406, 1986.

Grand, S. P., R. D. Van der Hilst, and S. Widiyantoro, Global seismic tomography: A snapshot of convection in the Earth, *GSA Today, 7*, 1-7, 1997.

Griffiths, R. W., and I. H. Campbell, Stirring and structure in mantle plumes, *Earth Planet. Sci. Lett., 99*, 66-78, 1990.

Griffiths, R. W., and M. A. Richards, The adjustment of mantle plumes to changes in plate motion, *Geophys. Res. Lett., 16*, 437-440, 1989.

Gurnis, M., Convective mixing in the Earth's mantle, Ph.D. thesis, Aust. Natl. Univ., Canberra, 1986.

Hager, B. H., and R. J. O'Connell, Kinematic models of large-scale flow in the Earth's mantle, *J. Geophys. Res., 84*, 1031-1048, 1979.

Hager, B. H., and R. J. O'Connell, A simple global model of plate dynamics and mantle convection, *J. Geophys. Res., 86*, 4843-4867, 1981.

Helmberger, D. V., L. Wen, and X. Ding, Seismic evidence that the source of the Iceland hotspot lies at the core-mantle boundary, *Nature, 396*, 251-255, 1998.

Hofmann, A. W., Mantle geochemistry: The message from oceanic volcanism, *Nature, 385*, 219-229, 1997.

Inokuchi, H., and F. Heider, Paleolatitude of the southern Kerguelen Plateau inferred from the paleomagnetic study of upper Cretaceous basalts, *Proc. Ocean Drill. Program Sci. Results, 120*, 89-96, 1992.

Ishii, M., and J. Tromp, Normal-mode and free-air gravity constraints on lateral variations in velocity and density of Earth's mantle, *Science, 285*, 1231-1236, 1999.

Jarrard, R. D., and D. A. Clague, Implications of Pacific island and seamount ages for the origin of volcanic chains, *Rev. Geophys., 15*, 57-76, 1977.

Kárason, H., R. D. van der Hilst, and K. Creager, Improving seismic models of global p-wave speed by the inclusion of core phases (abstract), *EOS Trans. AGU, 78*(46), Fall Meet. Suppl., F17, 1997.

Karato, S., Importance of anelasticity in the interpretation of seismic tomography, *Geophys. Res. Lett., 20*, 1623-1626, 1993.

Kuo, B.-Y., and K.-Y. Wu, Global shear velocity heterogeneities in the D" layer: Inversion from Sd-SKS differential travel times, *J. Geophys. Res., 102*, 11,775-11,788, 1997.

Kuo, C., J. J. Durek, and B. Romanowicz, Mantle heterogeneity inferred from normal mode spectra, *Eos Trans. AGU, 79*(45), Fall Meet. Suppl., F627, 1998.

Lambeck, K., and P. Johnston, The viscosity of the mantle: evidence from analyses of glacial-rebound phenomena, in *The Earth's Mantle*, edited by I. Jackson, pp. 461-502, Cambridge Univ. Press, New York, 1998.

Larsen, T. B., and D. A. Yuen, Fast plumeheads: Temperature-dependent versus non-Newtonian rheology, *Geophys. Res. Lett., 24*, 1995-1998, 1997.

Lee, D.-C., A. N. Halliday, J. G. Fitton, and G. Poli, Isotopic variations with distance and time in the volcanic islands of the Cameroon line: Evidence for a mantle plume origin, *Earth Planet. Sci. Lett., 123*, 119-138, 1994.

Leitch, A. M., G. F. Davies, and M. Wells, A plume head melting under a rifted margin, *Earth Planet. Sci. Lett., 161*, 161-177, 1998.

Li, X.-D., and B. Romanowicz, Global mantle shear velocity model developed using nonlinear asymptotic coupling theory, *J. Geophys. Res., 101*, 22,245-22,272, 1996.

Lithgow-Bertelloni, C., and M. A. Richards, The dynamics of Cenozoic and Mesozoic plate motions, *Rev. Geophys., 36*, 27-78, 1998.

Lithgow-Bertelloni, C., and P. G. Silver, Dynamic topography, plate driving forces and the African superswell, *Nature, 395*, 269-272, 1998.

Lonsdale, P., Geography and history of the Louisville Hotspot Chain in the southwest Pacific, *J. Geophys. Res., 93*, 3078-3104, 1988.

Loper, D. E., and F. D. Stacey, The dynamic and thermal structure of deep mantle plumes, *Phys. Earth Planet. Inter., 33*, 304-317, 1983.

MacDonald, G. A., *Volcanoes*, Prentice-Hall, Englewood Cliffs, N. J., 1972.

Manga, M., H. A. Stone, and R. J. O'Connell, The interaction of plume heads with compositional discontinuities in the Earth's mantle, *J. Geophys. Res., 98*, 19,979-19,990, 1993.

Masters, G., S. Johnson, G. Laske, and H. Bolton, A shear-velocity model of the mantle, *Philos. Trans. R. Soc. London, Ser. A, 354*, 1385-1411, 1996.

McClelland, L., T. Simkin, M. Summers, E. Nielsen, and T. C. Stein (Ed.), *Global Volcanism 1975-1985*, Prentice-Hall, Englewood Cliffs, N. J., 1989.

McNutt, M. K., D. W. Caress, J. Reynolds, K. A. Jordahl, and R. A. Duncan, Failure of plume theory to explain midplate volcanism in the southern Austral islands, *Nature, 389*, 479-482, 1997.

Mitrovica, J. X., Haskell [1935] revisited, *J. Geophys. Res., 101*, 555–569, 1996.

Mitrovica, J. X., and A. M. Forte, Radial profile of mantle viscosity: Results from the joint inversion of convection and postglacial rebound observables, *J. Geophys. Res., 102*, 2751–2769, 1997.

Molnar, P., and J. Stock, Relative motions of hotspots in the Pacific, Atlantic and Indian Ocean since late Cretaceous time, *Nature, 327*, 587-591, 1987.

Morgan, W. J., Convection plumes in the lower mantle, *Nature, 230*, 42-43, 1971.

Morgan, W. J., Deep mantle convection plumes and plate motions, *Am. Assoc. Pet. Geol. Bull., 56*, 203-213, 1972.

Morgan, W. J., Hotspot tracks and the opening of the Atlantic and Indian Oceans, in *The Sea*, vol. 7, *The Oceanic Lithosphere*, edited by C. Emiliani, pp. 443-487, John Wiley, New York, 1981.

Müller, R. D., J.-Y. Royer, and L. A. Lawver, Revised plate

motions relative to the hotspots from combined Atlantic and Indian Ocean hotspot tracks, *Geology, 21*, 275-278, 1993.

National Geophysical Data Center, Digital relief of the surface of the Earth, *Data Announc. 88-MGG-02*, Natl. Oceanic and Atmos. Admin., U.S. Dep. of Commer., Boulder, Colo., 1988.

Norton, I. O., Plate motions in the North Pacific: The 43 Ma nonevent, *Tectonics, 14*, 1080-1094, 1995.

O'Connor, J. M., and R. A. Duncan, Evolution of the Walvis Ridge-Rio Grande Rise hot spot system: Implications for African and South American plate motions over plumes, *J. Geophys. Res., 95*, 17,475-17,502, 1990.

O'Connor, J. M., and A. P. le Roex, South Atlantic hot spot-plume systems, 1, Distribution of volcanism in time and space, *Earth Planet. Sci. Lett., 113*, 343-364, 1992.

O'Connor, J. M., P. Stoffers, and M. O. McWilliams, Time-space mapping of Easter Chain volcanism, *Earth Planet. Sci. Lett., 136*, 197-212, 1995.

O'Connor, J. M., P. Stoffers, P. van den Bogaard, and M. McWilliams, First seamount age evidence for significantly slower African plate motion since 19 to 30 Ma, *Earth Planet. Sci. Lett., 171*, 575-589, 1999.

Panasyuk, S.V., B.H. Hager, and A. M. Forte, Understanding the effects of mantle compressibility on geoid kernels, *Geophys. J. Int., 124*, 121-133, 1996.

Phipps Morgan, J., W. J. Morgan, Y.-S. Zhang, and W. H. F. Smith, Observational hints for a plume–fed, suboceanic asthenosphere and its role in mantle convection, *J. Geophys. Res., 100*, 12,753-12,767, 1995.

Press, F., and R. S. Siever, *Earth*, W. H. Freeman, New York, 1986.

Ribe, N. M., and U. R. Christensen, The dynamical origin of Hawaiian volcanism, *Earth Planet. Sci. Lett., 171*, 517-531, 1999.

Ricard, Y., L. Fleitout, and C. Froidevaux, Geoid heights and lithospheric stresses for a dynamic Earth, *Ann. Geophys., 2*, 267-286, 1984.

Ricard, Y., M. A. Richards, C. Lithgow-Bertelloni, and Y. LeStunff, A geodynamic model of mantle mass heterogeneities, *J. Geophys. Res., 98* 21,895-21,909, 1993.

Richards, M. A., Hotspots and the case for a high viscosity lower mantle, in *Glacial Isostasy, Sea Level and Mantle Rheology, NATO ASI Ser. C*, vol. 334, edited by R. Sabadini, K. Lambeck, and E. Boschi, pp. 571-587, Kluwer Acad., Norwell, Mass., 1991.

Richards, M. A., and R. W. Griffiths, Deflection of plumes by mantle shear flow: Experimental results and a simple theory, *Geophys. J., 94*, 367-376, 1988.

Richards, M. A., and B. H. Hager, Geoid anomalies in a dynamic Earth, *J. Geophys. Res., 89*, 5987-6002, 1984.

Richards, M. A., B. H. Hager, and N. H. Sleep, Dynamically supported geoid highs over hotspots: Observation and theory, *J. Geophys. Res., 93*, 7690-7708, 1988.

Richards, M. A., R. A. Duncan, and V. E. Courtillot, Flood basalts and hot spot tracks: Plume heads and tails, *Science, 246*, 103-107, 1989.

Russell, S., T. Lay, and E. J. Garnero, Seismic evidence for small-scale dynamics in the lowermost mantle at the root of the Hawaiian hotspot, *Nature, 396*, 255-258, 1998.

Sager, W. W., and U. Bleil, Latitudinal shift of Pacific hotspots during the late Cretaceous and early Tertiary, *Nature, 326*, 488-490, 1987.

Schilling, J.-G., Fluxes and excess temperatures of mantle plumes inferred from their interaction with migrating mid-ocean ridges, *Nature, 352*, 397-403, 1991.

Schmincke, H. U., Vulkane und ihre Wurzeln, schriftenreihe, Akad. der Wissensch., Düsseldorf, Germany, 1982.

Sleep, N., Hotspots and mantle plumes: Some phenomenology, *J. Geophys. Res., 95*, 6715-6736, 1990.

Srivastava, S. P., Evolution of the Labrador Sea and its bearing on the early evolution of the North Atlantic, *Geophys. J. R. Astron. Soc., 52*, 313–357, 1978.

Steinberger, B. M., Motion of hotspots and changes of the Earth's rotation axis caused by a convecting mantle, Ph.D. thesis, 203 pp., Harvard Univ., Cambridge, Mass., Jan. 1996.

Steinberger, B., Slabs in the lower mantle–Results of dynamic modelling compared with tomographic images and the geoid, *Phys. Earth Planet. Inter.*, in press, 2000.

Steinberger, B., and R. J. O'Connell, Advection of plumes in mantle flow: Implications for hotspot motion, mantle viscosity and plume distribution, *Geophys. J. Int., 132*, 412–434, 1998.

Steinberger, B., and R. J. O'Connell, Effects of mantle flow on hotspot motion, in *The History and Dynamics of Global Plate Motions, Geophys. Monogr. Ser.*, edited by M. A. Richards, R. G. Gordon, and R. D. van der Hilst, AGU, Washington, D. C., in press, 2000.

Su, W.-J., R. L. Woodward, and A. M. Dziewonski, Degree 12 model of shear velocity heterogeneity in the mantle, *J. Geophys. Res., 99*, 6945-6980, 1994.

Suppe, J., C. Powell, and R. Berry, Regional topography, seismicity, Quarternary volcanism, and the present-day tectonics of the western United States, *Am. J. Sci., 275-A*, 397-436, 1975.

Tarduno, J. A., and R. D. Cottrell, Paleomagnetic evidence for motion of the Hawaiian hotspot during formation of the Emperor seamounts, *Earth Planet. Sci. Lett., 153*, 171-180, 1997.

Torsvik, T. H., R. D. Tucker, L. D. Ashwal, E. A. Eide, N. A. Rakotosolofo, and M. J. De Wit, Late Cretaceous magmatism in Madagascar: Palaeomagnetic evidence for a stationary Marion hotspot, *Earth Planet. Sci. Lett., 164*, 221-232, 1998.

Turcotte, D. L., and G. Schubert, *Geodynamics: Application of Continuum Physics to Geological Problems*, John Wiley, New York, 1982.

van Keken, P., Evolution of starting mantle plumes: A comparison between numerical and laboratory models, *Earth Planet. Sci. Lett., 148*, 1-11, 1997.

Watts, A. B., J. K. Weissel, R. A. Duncan, and R. L. Larson, Origin of the Louisville Ridge and its relationship to the Eltanin Fracture Zone System, *J. Geophys. Res., 93*, 3051-3077, 1988.

Wessel, P., and L. W. Kroenke, A geometric technique for relocating hotspots and refining absolute plate motions, *Nature, 387*, 365-369, 1997.

Wessel, P., and W. H. F. Smith, New version of the Generic Mapping Tools released, *Eos Trans. AGU, 76*, 329, 1995.

Whitehead, J. A., Instabilities of fluid conduits in a flowing Earth–Are plates lubricated by the asthenosphere?, *Geophys. J. R. Astron. Soc., 70*, 415-433, 1982.

Whitehead, J. A., and D. S. Luther, Dynamics of laboratory diapir and plume models, *J. Geophys. Res., 80*, 705-717, 1975.

Wilson, J. T., A possible origin of the Hawaiian islands, *Can. J. Phys., 41*, 863-870, 1963.

Wood, C. A., and J. Kienle, *Volcanoes of North America*, Cambridge Univ. Press, New York, 1990.

B. Steinberger, Institut für Meteorologie und Geophysik, Johann Wolfgang Goethe-Universität, Feldbergstr. 47, 60323 Frankfurt am Main, Germany. (steinber@geophysik.uni-frankfurt.de)

(Received March 3, 1998; revised October 28, 1999; accepted November 5, 1999.)